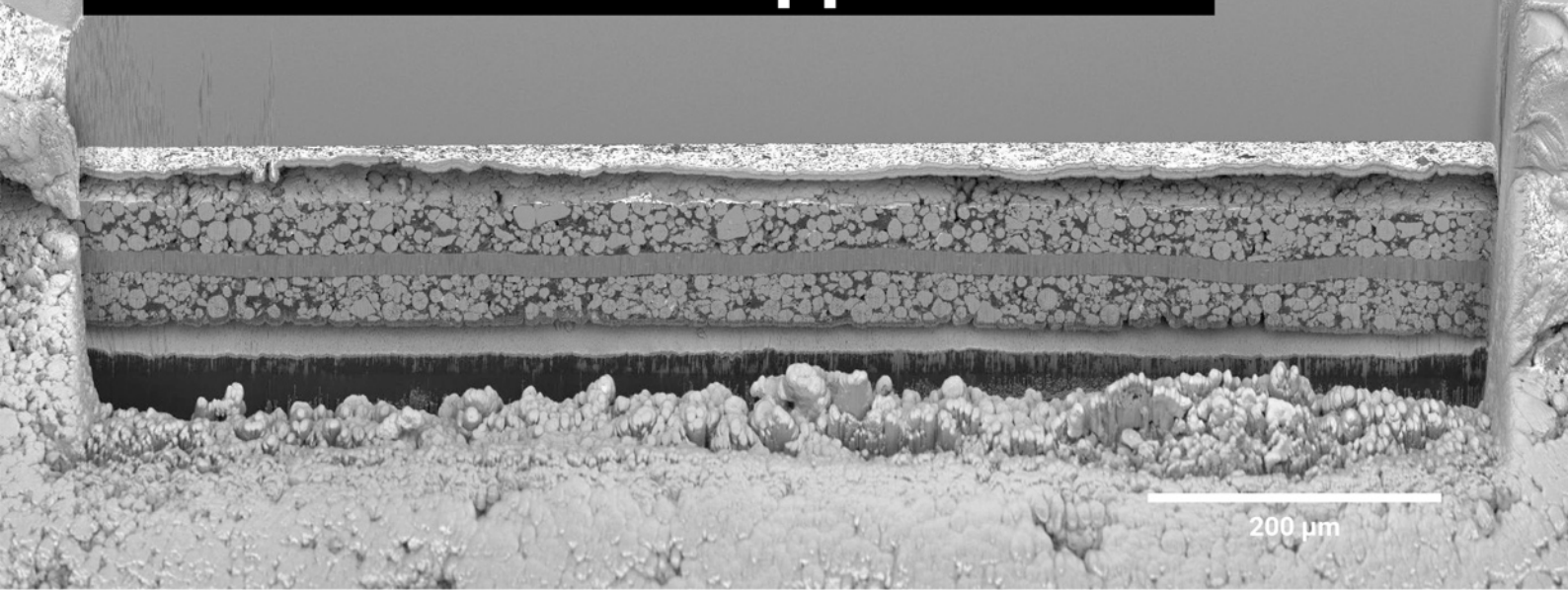


A unique combination of Plasma FIB and field-free UHR SEM for the widest range of multiscale materials characterization applications



1 mm cross-section through a Li-ion battery electrode

TESCAN AMBER X

- ✓ High throughput, large area FIB milling up to 1 mm
- ✓ Ga-free microsample preparation
- ✓ Ultra-high resolution, field-free FE-SEM imaging and analysis
- ✓ In-column SE and BSE detection
- ✓ Spot optimization for high-throughput, multi-modal FIB-SEM tomography
- ✓ Superior field of view for easy navigation
- ✓ Essence™ easy-to-use, modular graphical user interface



For more information visit

www.tescan.com

Surface Reconstruction of Water Splitting Electrocatalysts

Ye Zeng, Mengting Zhao, Zihao Huang, Weijie Zhu, Jiaxian Zheng, Qiu Jiang,*
Zhoucheng Wang, and Hanfeng Liang*

Water electrolysis is regarded as an efficient and green method to produce hydrogen gas, a clean energy carrier that holds the key to solving global energy problems. So far, the efficiency and large-scale application of water electrolysis are restricted by the electrocatalytic activity of applied catalysts. Recently, the reconstruction phenomenon of electrocatalysts during a catalytic reaction has been discovered, which could form reactive sites for both the oxygen evolution and hydrogen evolution reactions. Regulation of the reconstruction process to generate a large number of reactive species with high activity has since been demonstrated as an effective strategy to enhance the catalytic performance of electrocatalysts. This review summarizes recent progress in the regulation strategies for reconstruction reactions. First, the mechanism of water electrolysis is briefly introduced, and the critical factors regarding the reconstruction process are systematically discussed, followed by a brief introduction of advanced characterization for reconstruction. Moreover, the modulation strategies are summarized with reported examples highlighting the promoted effects on the reconstruction process. Finally, the challenges facing surface-reconstructed catalysts for water electrolysis in the future are discussed.

Gibbs free energy (ΔG) of water splitting reaction is $237.2 \text{ kJ mol}^{-1}$, corresponding to a theoretical voltage of 1.23 V .^[3] However, the existence of electrochemical/concentration polarization and solution resistance can increase the actual voltage of water electrolysis to much beyond 1.23 V . Particularly, the OER involves a complicated four-electron transfer process, which results in a sluggish kinetics thus has long been the bottleneck.^[4] Therefore, it is necessary to explore efficient and robust electrocatalysts to reduce the overpotential of water electrolysis and the extra electric energy consumption. Although noble electrocatalysts, such as Pt, RuO_2 and IrO_2 , are recognized as the most efficient electrocatalysts for water electrolysis, their high scarcity and instability severely impede large-scale applications.^[5] Recently, considerable effort has been focused on non-noble transition-metal materials as viable alternatives for water splitting. Understanding the intrinsic catalytic mechanism

1. Introduction

As a clean energy carrier, hydrogen has the potential to solve the energy crisis.^[1] Water electrolysis has been regarded as one of the most efficient methods to produce hydrogen gas with high purity. The process contains two half-reactions, namely the hydrogen evolution reaction (HER) on the cathode and the oxygen evolution reaction (OER) on the anode.^[2] The standard

and real active sites of these catalysts will benefit the rational design and application of high-efficiency catalysts.

With the development of in situ characterization technologies, more reports have revealed that the original electrocatalyst (so-called “pre-catalyst”) surface sites would undergo dynamic reconstruction and transform into real reactive species.^[6] This in situ reconstruction process could tune the electrocatalytic behaviors such as adsorption, activation, and desorption, thus improving the catalytic performance.^[7] On this basis, many researchers utilized the pre-reconstruction of electrocatalysts to obtain a large number of active species for the catalytic reactions.^[8] It has been found that the intrinsic properties of the pre-catalysts, such as composition, atomic arrangement, porosity, and crystallinity, would affect the reconstruction rate, reconstruction degree, and catalytic activity of the reconstructed species.^[9] Moreover, the reaction conditions also affect the reconstruction process, such as electrochemical operation, applied potential, electrolyte concentration, and pH.^[6a] Therefore, tuning the reconstruction process to generate abundant active sites with high intrinsic activity is an effective strategy to boost the catalytic performance of electrocatalysts.

Although some influential review articles on the reconstruction of catalysts during water electrolysis have emerged,^[10] most of them focus on the discovery and characterization of the reconstruction phenomenon, less on the regulation of the reconstruction process. In addition, reconstructed catalysts for

Y. Zeng, M. Zhao, Z. Huang, W. Zhu, J. Zheng, Z. Wang, H. Liang
State Key Laboratory of Physical Chemistry of Solid Surfaces
College of Chemistry and Chemical Engineering
Xiamen University
Xiamen 361005, China
E-mail: hfliang@xmu.edu.cn

Q. Jiang
School of Materials and Energy
University of Electronic Science and Technology of China
Chengdu 611731, China
E-mail: jiangqiu@uestc.edu.cn

H. Liang
Innovation Laboratory for Sciences and Technologies of
Energy Materials of Fujian Province (IKKEM)
Xiamen 361005, China

 The ORCID identification number(s) for the author(s) of this article can be found under <https://doi.org/10.1002/aenm.202201713>.

DOI: 10.1002/aenm.202201713

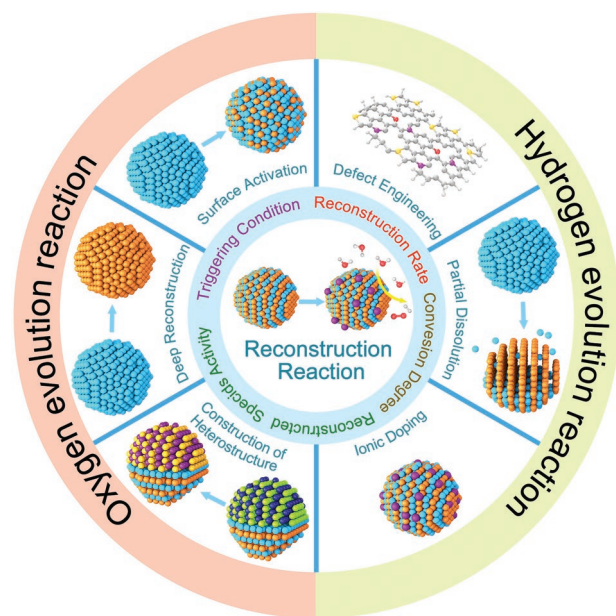


Figure 1. Schematic illustration of the modulation strategy of reconstruction for oxygen evolution reaction and hydrogen evolution reaction.

HER have seldom been discussed, which is an important topic since the reasonable regulation of the reconstruction process is the key to improving the activity of the reconstructed electrocatalysts. Thus, this timely review summarizes the modulation strategies that promote the reconstruction process to enhance the number and OER/HER activity of newly formed active species. As shown in **Figure 1**, the regulation strategies could be classified into six categories: surface activation, defect engineering, partial dissolution of pre-catalysts, ionic doping, construction of heterostructures, and deep reconstruction. These regulation strategies would influence the triggering condition, reconstruction rate, conversion degree, and the reconstructed species' catalytic activity. In addition, we also generalized a series of physicochemical characteristics applied in tracking the dynamic reconstruction process and revealing real active sites. Through this review, we hope to provide insights on the design and preparation of reconstructed electrocatalysts for the benefit of the readers that are interested in this emerging field.

2. Fundamentals of Water Electrolysis

A complete electrolyzer for overall water splitting should consist of a power source, electrolyte, a cathode, and an anode.^[11] When voltage is applied, the water molecules in the electrolyzer will decompose to form oxygen and hydrogen.^[12] As a half-reaction on the cationic electrode, the HER undergoes a Volmer reaction followed by Heyrovsky or Tafel reaction,^[13] as displayed in **Figure 2a**. For the Volmer reaction in acidic solution, free H^+ will be adsorbed on the catalyst's active sites and combined with an electron transferred from the electrode surface, and thus be transformed into hydrogen atoms bonded with metal sites (M-H). The generated hydrogen atoms (H_{ads}) could form hydrogen molecules (H_2) through Heyrovsky or Tafel reaction in the subsequent HER process. In the Heyrovsky reaction,

electrons from the electrode surface combine with M-H and free H^+ in the solution to form H_2 molecules, which are then desorbed from the electrode surface. In the Tafel reaction, the H_2 molecules are formed by combining two hydrogen atoms adsorbed on the electrode surface and then break away from the active sites. In alkaline electrolytes, the H_{ads} adsorbed on the catalyst's surface originate from the breakage of water molecules due to the low proton concentration. Hence, the alkaline HER process requires more activation energy. In the actual reaction, the reaction path might follow Volmer-Heyrovsky, Volmer-Tafel, or both. No matter which reaction mechanism the HER reaction follows, the adsorption and desorption of H_{ads} play a crucial role in the reaction rate. The weak binding bonds between H_{ads} and the active sites would lead to reduced adsorption of H_{ads} on the catalyst surface and prevent the reaction from continuing. Whereas the strong binding bonds would make it difficult for the desorption of H_2 molecules from the catalyst surface. The binding bonds could be estimated by calculating the adsorption free energy (ΔG_H) of H_{ads} on the catalyst surface.^[14] For ideal HER catalysts, the adsorption free energy should be close to 0, that is, not too strong nor too weak.^[15] Pt and Pt-based catalysts have been proved to be the best HER catalysts at present due to their optimal ΔG_H .^[16] However, their high cost and scarcity limit the practical application. Transitional metals (W, Co, Ni, etc.) and their derivatives (phosphides, sulfides, and selenides, etc.) with significantly reduced cost have been regarded as promising alternatives.^[17] Although there is still a big gap between their performance and that of Pt-based catalysts, the existing design and modulation strategies (single-atom catalysts,^[18] atomic defect engineering,^[19] heteroatoms doping,^[20] and heterostructure design^[21]) have shown the efficacy of enhancing the electrocatalytic performance, aiming to approach the HER performance of Pt-based catalysts.

The OER process involves many complex elementary reactions with intricate electron and proton transfer processes.^[22] The dynamic evolution of reactive sites on the surface during the OER process brings about additional difficulty in identifying the reaction mechanism. Figure 2b shows one of the widely recognized reaction mechanisms at present. Taking the alkaline OER as an example, free OH^- in solution is adsorbed on the active site of catalyst to form R-OH intermediate accompanied by transferring an electron from OH^- to the electrode, which is then oxidized to M-O. The M-O subsequently binds with another OH^- to form the M-OOH, which is then oxidized to release oxygen molecules.^[5b] Compared with the alkaline OER process, the acidic OER process requires additional energy to promote water dissociation.^[23] The OER process often involves the adsorption and desorption of oxygen-containing intermediates on catalysts; thus the catalysts applied for OER tend to be transition metal oxides, hydroxides,^[24] and high-valence metal salts with oxygen-containing functional groups. In addition, the catalyst would undergo violent oxidation during the OER process. Therefore, some easily oxidizable catalysts could also show excellent catalytic performance, such as transition metal phosphides,^[25] selenides,^[26] and sulfides.^[27] The most critical indicator for OER activity is the bonding strength of M-O in the intermediate groups during the OER process. The weak M-O bond strength would lead to the difficult formation of the intermediate groups, while the strong M-O bond strength would

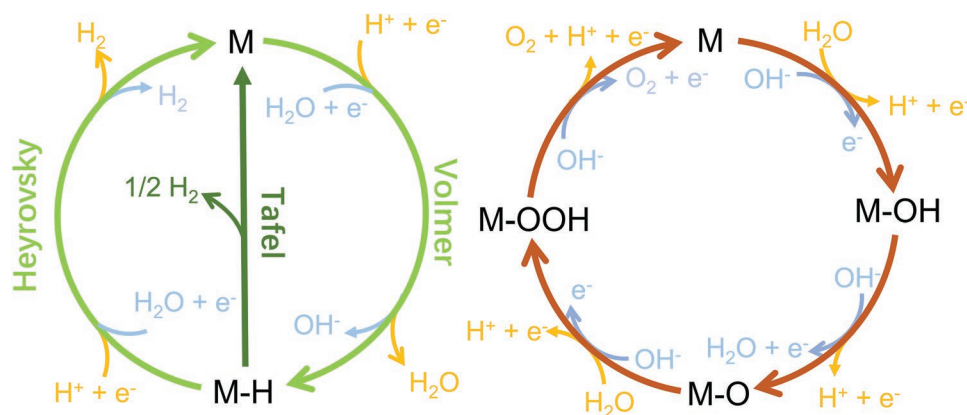


Figure 2. Mechanism of a) hydrogen and b) oxygen evolution reactions in acidic (orange) and alkaline (blue) solution.

make the intermediate groups too stable, which is not conducive to the next reaction.

During both the OER and HER, the active sites play an important role in the adsorption and desorption of intermediates, and therefore determine the activity of the catalysts. In most cases, the generation of highly active sites is usually accompanied by dynamic surface reconstruction. Therefore, understanding the dynamic reconstruction process of catalysts during the catalytic reaction is significant for revealing the intrinsic catalytic mechanism and the real active species of catalysts.

3. Reconstruction of Electrocatalysts

3.1. Reconstruction Phenomenon

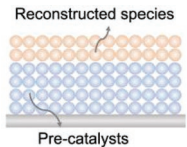
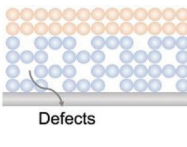
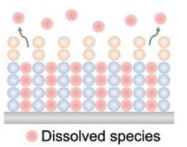
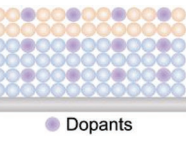
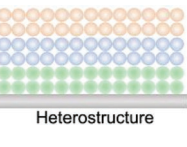
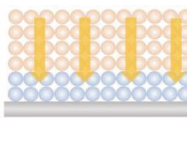
Generally speaking, the reconstruction phenomenon refers to the evolution in structures of electrocatalysts during the reaction process. As with the development of in situ characterization techniques to detect the fine structure on the catalyst surface,^[28] the reconstruction process can now be observed under electrochemical conditions. During electrochemical reconstruction, pre-catalysts would be transformed into amorphous or low-crystallinity active species.^[29] In most reports, the dynamic reconstruction could tune the catalytic performance of catalysts, which can significantly reduce the energy required for water oxidation. In addition, several reports also have shown that the pre-catalysts could also undergo reconstruction under HER condition, causing local atomic rearrangement and the reduction of high-valence metal cation,^[30] which benefit the HER process. The reconstruction reaction can be evaluated in terms of triggering condition, reconstruction rate, and conversion degree. Triggering condition refers to the potential, such as temperature, electrolyte concentration and overpotential, at which reconstruction occurs. Under certain temperature and electrolyte, reducing the starting potential allows generation of reactive sites at low potential, which can then initiate the HER/OER at low overpotentials. The reconstruction rate represents the difficulty level of driving the reconstruction process. Accelerating the reconstruction rate can create rich active sites quickly, which is conducive to the improvement in water electrolysis

efficiency. Reconstruction degrees could reflect the conversion rate of pre-catalysts. Enhancing the degree of reconstruction can convert more pre-catalyst components into active species, leading to deeper reconstructed layer, a large number of active sites, and a high utilization rate of pre-catalyst. Since the reconstruction process is essentially a chemical reaction, the intrinsic properties of the pre-catalyst along with the reconstruction conditions would affect the reconstruction process. In addition, the dynamic structural evolution would tune the intrinsic properties (e.g., composition, microstructures, metal valence state, defect level) of newly formed species, which are related to the catalytic performance.^[31] Hence, tuning the intrinsic properties of the pre-catalyst and applying reasonable reconstruction strategies such as surface activation, defect engineering, partial dissolution, ionic doping, heterostructure construction, and deep reconstruction, could tune the reconstruction behavior and thus the structure of the pre-catalyst, and thereby boosting the catalytic activity of the reconstructed layers. The most common driving force for the reconstruction through various strategies is essentially the surface chemical reactions or chemical conversions (except for the partial dissolution), which often result in the formation of new electrocatalytically active species. To promote the reconstruction, the catalysts could be designed with high surface area (which benefits the surface activation), high structural feasibility (e.g., through defect engineering), or high electronic/ionic transport properties (e.g., through ionic doping or heterostructure construction). These strategies, however, could deliver different reconstruction results as they focus on the modification of different specific properties of the pre-catalysts, and would thus possess distinct impacts on the reconstruction kinetics, reconstruction pathway, and reconstruction degree. **Table 1** illustrates the effective reconstruction strategies along with the related catalytic systems. The application of these modulation strategies in promoting the reconstruction of OER and HER catalysts would be discussed in more detail in Sections 4 and 5, respectively.

3.2. Advanced Characterizations

The information on reconstruction can be obtained through a series of ex situ and in situ electrochemical, electron

Table 1. Summary of the reconstruction strategies and typically associated systems.

Reconstruction strategies					
Surface activation	Defect engineering	Partial dissolution	Ionic doping	Heterostructure construction	Deep reconstruction
 <p>Reconstructed species</p> <p>Pre-catalysts</p>	 <p>Defects</p>	 <p>Dissolved species</p>	 <p>Dopants</p>	 <p>Heterostructure</p>	
Typical systems					
Non-oxide catalysts with large surface area.	Catalysts with abundant defects.	Catalysts with soluble species in electrolytes.	Catalysts with elemental dopants.	Hybrid catalysts with a heterostructure.	Catalysts with electrochemically unstable structure.
Example: CoP nanosheets, Ni ₂ Mo ₃ N nanorods	Example: Co ₃ O ₄ with oxygen vacancies	Example: NiGa LDH in KOH, SrIrO _x in H ₂ SO ₄	Example: Cl-doped LiCo ₂ O ₄ , Fe-doped CoAl ₂ O ₄	Example: Pd/Fe ₃ O ₄ , Co ₃ O ₄ /CeO ₂	Example: Metal-organic frameworks, metal molybdates

microscopic, X-ray diffraction (XRD) and spectroscopic characterizations. Ex situ techniques can capture the structural and component properties of pre-catalysts; however, it is challenging to obtain detailed information during the catalytic reaction. Whereas in situ techniques are capable of tracking the evolution of catalysts in real-time (e.g., changes in metal valence state and atomic structure transition), which gives important data for further understanding the reconstruction mechanism and designing high-performance pre-catalysts.^[32] A variety of ex situ and in situ characterization techniques are systematically discussed as follow.

The number of reconstructed species and electrocatalytic activity evolve as the reconstruction proceeds, which can change the electrochemical properties reflected by electrochemical characterization techniques. For example, the evolution in the curve shape of cyclic voltammetry (CV) during reconstruction could determine the reversibility of the electrode reaction, the adsorption of intermediates, and the formation of new phases.^[10a] As shown in **Figure 3a**,^[33] the area under the oxidation peaks of reduced graphene oxide (Ni_{1.4}Fe_{0.6}P@rGO) catalyst gradually enlarges with the ongoing CV test, suggesting the successive formation of reconstructed NiOOH active species on the catalyst surface. In addition, the variation of catalytic activity can be reflected by the linear sweep voltammetry (LSV) curve and chronopotentiometry (CP), which directly show the changing trend of catalytic current density during the reconstruction process. For instance, **Figure 3b** shows that the overpotential of Ni_{1.4}Fe_{0.6}P@rGO to drive an OER current density of 10 mA cm⁻² gradually decreases during the first ten cycles, implying the enhancement in OER activity. The increasing current density can also be observed in the surface reconstruction of Co_xO_y/FTO under chronopotentiometry operation (**Figure 3c**),^[34] which represents the enhancement in OER performance due to the formation of active sites. The reconstruction process could optimize pre-catalysts' surface properties and electronic structure to accelerate the electron transfer rate, as can be reflected by in situ electrochemical impedance spectroscopy (EIS) analysis. For example, Wang et al. applied in situ EIS characterization to trace the evolution of Co-active sites in

oxygen deficient Co₃O₄ during OER.^[35] As shown in **Figure 3d**, the decrease of charge transfer resistance (R_{ct}) represents the reduction in the OH⁻ adsorption resistance. However, the evolution in structure and composition during reconstruction cannot be reflected intuitively by electrochemical characterization.

The reconstruction often leads to the morphological changes of the catalysts, which can be observed using microscopy. These changes, sometimes can be directly observed by the scanning electron microscopy (SEM), for instance, the formation of FeNi oxyhydroxide layer on the Fe_{0.4}Ni_{0.6}-alloy surface after the OER (**Figure 3e,f**).^[36] However, in most cases, the SEM techniques fail to reveal the specific information of the ultrathin reconstructed layer on the surface and the internal structure evolution of catalysts. Transmission electron microscope (TEM) is another common tool to study microstructures; it works by producing images based on the transmitting electron beam crossing samples.^[39] Compared with the SEM technique, TEM is able to explore both the surface evolution and interior structure. Tarascon et al. conducted high resolution TEM (HRTEM) accompanied with the fast Fourier transform (FFT) characterization of La₂LiIrO₆ with different activation cycles.^[37] **Figure 3g** reveals the growth process of IrO₂ nanoparticles on the catalyst surface along with the evolution of lattice during electrochemical activation. In addition, the reconstruction process can be observed in real-time using in situ TEM characterization. As displayed in **Figure 3h**, Ersen et al. observed the phase conversion of crystalline Co₃O₄ nanoparticles into amorphous CoO_xH_y, a composite of crystalline CoO, CoOOH, and Co(OH)₂ through operando TEM characterization.^[38] This technique can be applied during the catalytic reaction, thus deserves more attention in reconstruction research.

X-ray diffraction uses the X-ray with a specific wavelength to irradiate the sample. The atoms in the sample excite secondary X-rays and interfere with each other to produce specific diffraction.^[40] The phase structure and crystal size of bulk electrocatalysts can be revealed through the analysis of the diffraction pattern. For example, in situ XRD patterns of Ni(OH)₂ confirm through the appearance of strong peaks assigned to γ -NiOOH of its existence at certain potentials (**Figure 4a**).^[41] Although XRD techniques show the advantages of fast detection and simple

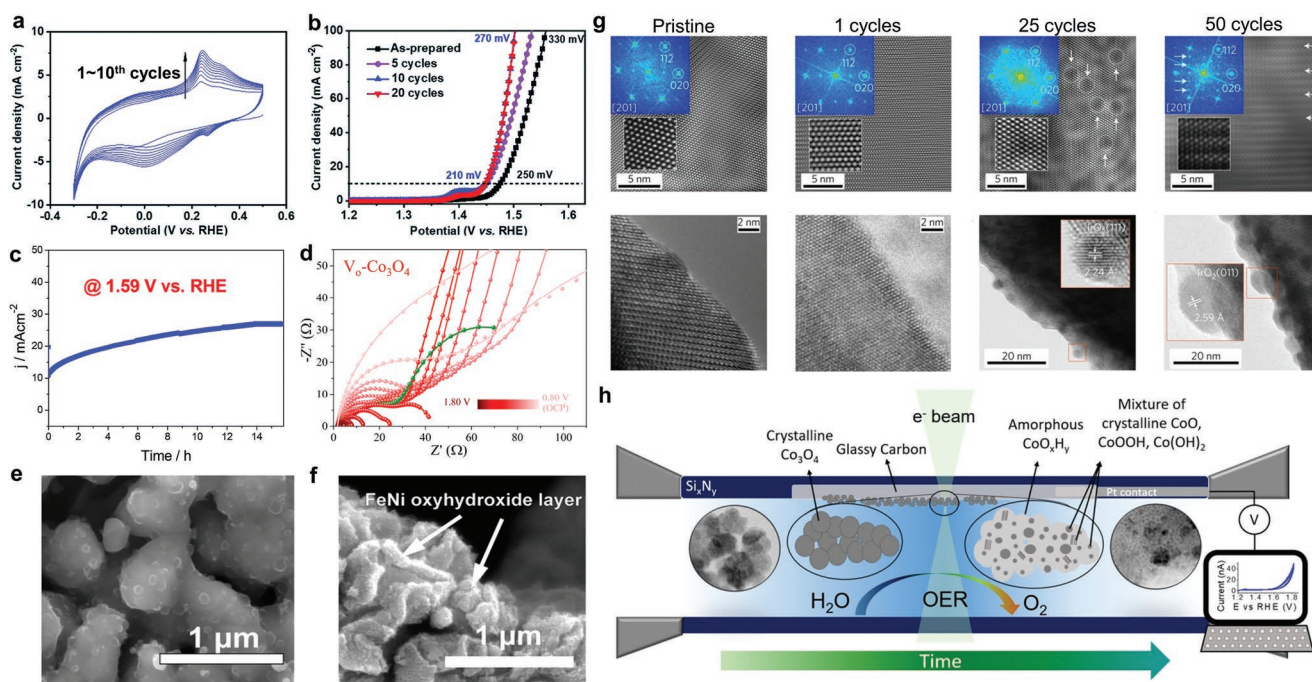


Figure 3. a) Continuous CV and b) LSV polarization curves of the $\text{Ni}_{1.4}\text{Fe}_{0.6}\text{P@rGO}$ catalyst in 1 M KOH. Reproduced with permission.^[33] Copyright 2019, Royal Society of Chemistry. c) Chronoamperometric activation curves of $\text{Co}_3\text{O}_4/\text{FTO}$ in 1 M KOH. Reproduced with permission.^[34] Copyright 2017, Royal Society of Chemistry. d) In situ measured EIS spectra of $\text{V}_6\text{-Co}_3\text{O}_4$ catalysts in 1 M KOH. Reproduced with permission.^[35] Copyright 2020, American Chemical Society. SEM images of $\text{Fe}_{0.4}\text{Ni}_{0.6}$ -alloy fiber paper e) before and f) after OER tests. Reproduced with permission.^[36] Copyright 2021, Elsevier. g) FFT filtered HRTEM images of La_2LiR_6 at different cycling times. Reproduced with permission.^[37] Copyright 2016, Springer Nature. h) Illustration of the evolution of Co_3O_4 nanoparticles during OER process as revealed by in situ TEM. Reproduced with permission.^[38] Copyright 2019, American Chemical Society.

operation, they are unable to accurately detect the evolution of surface reconstructed species with an amorphous state. X-ray photoelectron spectroscopy (XPS) applies characteristic X-ray to interact with atoms on the surface of the sample and induce electron ionization in the inner shell of the atom to release photoelectron.^[42] The surface (and a few nanometers near the surface) composition and chemical states of catalysts could be accurately determined by measuring the kinetic energy of the photoelectron with good spectra repeatability. Qiu et al. uncovered the intensity increasing trend of the XPS peaks assigned to Co^{3+} and M-O along with the decay of P peak in operando XPS spectra of $\text{Co}_{0.8}\text{Fe}_{0.2}\text{P@C}$ during electrochemical activation (Figure 4b),^[43] confirming the formation of active CoOOH species accompanied with the leaching of P. Since XPS characterization is very sensitive to the catalyst surface composition and susceptible to impurities, it must be conducted in conjunction with ion etching to realize depth analysis of the sample. In addition, low-energy ion scattering (LEIS) is also a powerful technique that can be used to analyze the surface chemical and structure makeup of the catalysts.^[44] The LEIS involves an ion beam (typically with a low energy of 0.1–10 keV) directed at the samples and the collection of energy spectra of scattered ions. The LEIS has a very high sensitivity to the elemental composition of the outermost atomic layer of a material, which cannot be realized by other surface sensitive techniques such as XPS. Further, the LEIS can also provide depth profile information of ≈ 10 nm. Unfortunately, this technique has rarely been applied

to study the reconstruction of electrocatalysts.^[45] Due to its extremely high sensitivity, the LEIS requires ultra-high vacuum conditions and the signal could be blocked by unexpected surface contaminations. Fourier-transform infrared spectroscopy (FTIR) is conducted by achieving the transitions of vibrational and rotational energy levels from the ground state to the excited state under the continuous change of infrared light. From analyzing the generated molecular absorption spectrum, composition and structure of functional groups of the newly formed species during the reconstruction process can be identified.^[46] For instance, Xia et al. confirmed the formation of metal oxyhydroxide during the OER by performing operando attenuated total reflection FTIR (ATR-FTIR) (Figure 4c).^[47] However, the relatively low sensitivity of FTIR requires higher content of detected components in samples.

The top surface information of catalysts during electrocatalysis can be also gained by Raman spectroscopy combined with probing molecules, which could reflect the evolution of chemical bonds and groups in the bulk catalysts with high sensitivity.^[50] Lin et al. noted the formation of active species is potential-dependent,^[48] as shown in Figure 4d. The Raman peaks at 474 and 554 cm^{-1} could be assigned to $\gamma\text{-NiOOH}$, which would appear as the potential increased to 1.41 V, indicating the formation of Ni^{3+} active species on the surface. Nevertheless, overlap of different vibration peaks and Raman scattering intensity are easily affected by optical system parameters. The structural evolution of the reconstructed species formed on the electrocatalysts

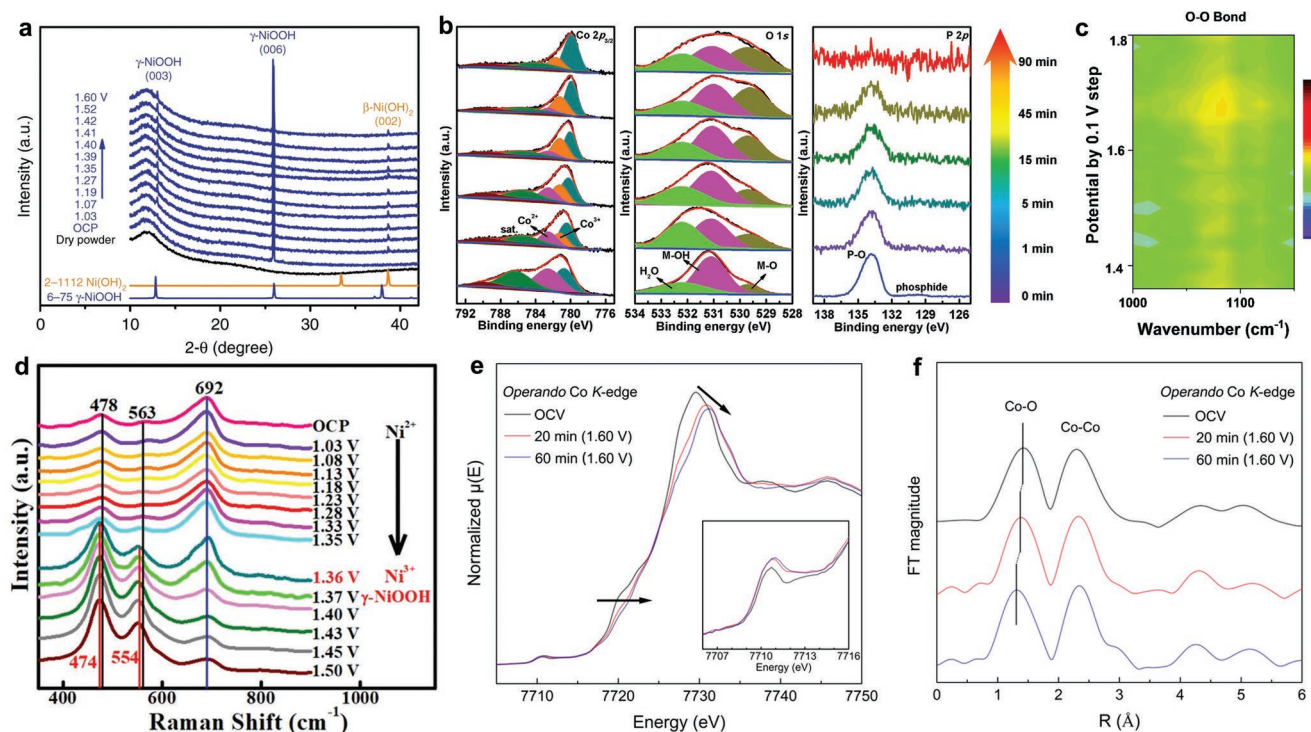


Figure 4. a) In situ XRD patterns of Ni(OH)₂/NF for the OER. Reproduced with permission.^[41] Copyright 2018, Springer Nature. b) In situ XPS spectra of Co 2p, O 1s, and P 2p of Co_{0.8}Fe_{0.2}P@C after different activation time. Reproduced with permission.^[43] Copyright 2020, Wiley-VCH. c) In situ ATR FTIR spectrum of dealloyed multiple-metal-site alloy under OER condition. Reproduced with permission.^[47] Copyright 2020, Royal Society of Chemistry. d) In situ Raman spectra of NiFe₂O₄/NF at different potentials. Reproduced with permission.^[48] Copyright 2021, National Academy of Sciences. e) In situ XANES and f) corresponding FT-EXAFS spectra of Li₂Co₂O₄ after 20 and 60 min. Reproduced with permission.^[49] Copyright 2019, American Chemical Society.

could be monitored by X-ray absorption spectroscopy (XAS), which is very sensitive to the variation in local chemical environments of bulk catalysts,^[51] in which the sample absorbs X-rays to excite its core electrons to vacant orbitals (XANES) or to the continuous state to form dry emission waves (EXAFS) with surrounding atoms. XANES spectra can reflect the chemical valence states and electronic structure, while the bond distances and coordination numbers around adjacent atoms can be calculated from EXAFS result. For example, Li et al. used the in situ XAS technique to track the spontaneous delithiation during the reconstruction process.^[49] Figure 4e shows a positive shift and decreased intensity of Co K-edge XANES spectra after the OER, indicating an increase in the cobalt valence state. Moreover, the variation of Co K-edge EXAFS spectra (Figure 4f) reflects the shrinkage of Co-O distance and increasing Debye-Waller factor, confirming a distortion of the CoO₆ octahedron. The technique can track the dynamic structural evolution of bulk electrocatalysts in terms of the coordination environments and average oxidation states, thus can accurately detect the structure of disordered or amorphous reconstructed species. However, the results of XAS are easily affected by mutual element interference and superposed peaks. Finally, all mentioned techniques for ex situ and in situ characterizations of the reconstruction process and their respective information obtained as well as advantages and disadvantages are summarized in Table 2 for comparison.

4. Reconstruction Strategies for OER Electrocatalyst

The reconstruction of pre-catalysts leads to the formation of real active catalytic sites that determine the OER performance. The modification of reconstruction process can tune the intrinsic structural properties of reconstructed layers and thus the electrocatalytic activity. In this section, modification strategies, including surface activation, defect engineering, partial dissolution, ionic doping, heterostructure construction and deep reconstruction, will be systematically discussed to reveal how they can be applied to tune the reconstruction process and the structure of reconstructed species that lead to high catalytic activity.

4.1. Surface Activation

The surface reconstruction of pre-catalysts could be achieved by electrochemical activation. Electrochemical activation is a common method to induce structural changes in pre-catalysts, such as surface oxidation, ion leaching, and phase transformation.^[52] The surface evolution is affected by the applied electrochemical operation conditions, such as continuous cycling, galvanostatic, and potentiostatic states. Subramanian et al. have explored the influence of different electrochemical operations

Table 2. Summary of characterizations for the reconstruction.

Advanced characterizations for reconstruction										
Electrochemical characterization			Electron microscopic characterization			X-ray diffraction and spectroscopic characterization				
CV	LSV/CP	EIS	SEM	TEM	XRD	XPS	FITR	Raman	XAS	LEIS
Characterization sites										
Bulk	Bulk	Bulk	Surface	Bulk	Bulk	Surface or near surface	Bulk	Bulk	Bulk	Surface or near surface
Information obtained for measured samples										
Electrode reaction and reversibility	Electro-catalytic activity	Electrode reaction kinetics and internal resistance	Surface morphology	Surface morphology and hyperfine structure	Phase structure and crystal size	Elemental composition and chemical valence states	Group composition and molecular structure	Chemical bonds and groups	Coordination environments	Chemical and structure makeup
Pros										
Intuitively reflecting the dynamic change of electrochemical properties			Stereoscopic and wide-field imaging	High resolution and easy to reflect hyperfine structure	Fast detection and simple operation	High sensitivity and good spectra repeatability	High penetration and no loss of samples	High sensitivity and short test time	High analytical precision and wide applicability	High sensitivity to both structure and composition of surface
Cons										
Failing to reflect evolution in structure and composition during reconstruction			Low resolution and inability to show fine structure	Limited imaging range	Failing to test amorphous structure	Susceptible to surface impurities	Poor sensitivity and difficult analysis	Susceptible to optical parameters	Susceptible to mutual elements interference and superposed peaks	Unexpected surface contamination could block the signal of real species

on the surface activation of Co_xO_y .^[34] As shown in **Figure 5a**, the CV curves obtained before and after activation confirm the notable reduction in overpotential at 10 mA cm^{-2} achieved by both galvanostatic and potentiostatic methods, which contributes to the formation of $\beta\text{-CoOOH}$ on the surface, and the effect of potentiostatic method is more remarkable. In addition, electrochemical cycling has been an effective method to promote the irreversible transformation of the pre-catalysts. The less stable components would leach gradually into the electrolyte during continuous cycling until stable species form on the surface. Xu et al. recently applied the electrochemical delithiation achieved by electrochemical cycling as an efficient strategy to convert LiNiO_2 pre-catalyst into highly active NiOOH as catalytic sites for OER.^[53] **Figure 5b** exhibits that the NiOOH layers are formed on the surface accompanied by contraction of Ni-O bonds induced by migration of Ni with the aid of electrochemical delithiation. Electron energy loss spectroscopy (EELS) and XAS characterization reflect the surface evolution of LiNiO_2 with prolonged CV cycling. As shown in **Figure 5c**, the EELS result suggests a higher Ni intensity of LiNiO_2 treated by 500 cycles (LNO-500) than that of original LiNiO_2 , indicating that Ni accumulates on the surface during activation cycling. **Figure 5d** reveals the increase in Ni valence state and Ni-O shrinkage with prolonged activation cycles, suggesting the formation of $\gamma\text{-NiOOH}$ on the delithiated LiNiO_2 . Such evolution of NiOOH on the surface correlates with the high OER activity. The rich Li vacancies in delithiated LiNiO_2

created by electrochemical delithiation could promote the deprotonation of NiOOH to form NiOO^* during the OER process, which serves as electrophilic centers to boost the OER. It can be noted that the OER current density of LiNiO_2 retains the tendency to increase from 1st to 500th, and subsequently decreases from 500th to 1000th (**Figure 5e**), implying that the double-edged sword effect of activation cycles on the OER performance. Therefore, attention should be paid to the influence of cycle number on the structure and catalytic activity of the reconstructed species catalyst during CV activation.

In addition to the number of cycles, the surface evolution of catalysts is also influenced by the potential range of cycling. Xia et al. revealed the formation of $\text{FeH}_9(\text{PO}_4)_4$ (FePi) on the surface of $\text{Ni}_{1.4}\text{Fe}_{0.6}\text{P}$ decorated on reduced graphene oxide ($\text{Ni}_{1.4}\text{Fe}_{0.6}\text{P}@r\text{GO}$) through cycling at a potential range of -0.3 – 0.5 V versus RHE for 10 cycles.^[33] HRTEM image (**Figure 5f**) confirms the formation of a crystalline phosphate layer between $\text{Ni}_{1.4}\text{Fe}_{0.6}\text{P}$ and rGO shell, resulting in enhanced OER activity due to the FePi/ $\text{Ni}_{1.4}\text{Fe}_{0.6}\text{P}$ synergy. Besides, they found that the phosphate disappeared whereas NiFe-OH formed at a higher potential range of 1.2 – 1.5 V versus RHE. Similarly, Huang et al. adjusted the applied potential of continuous cycling to tune the dealloying of IrTe_2 hollow nanoshuttles (HNSs).^[54] At low potentials, the Te was partially leached off, leading to IrTe_2 HNSs with a metallic Ir shell along with abundant defects (D-IrTe_2), whereas at higher potentials, the surface Ir was further oxidized into IrO_x (**Figure 5g**). The HRTEM images reveal rich defects

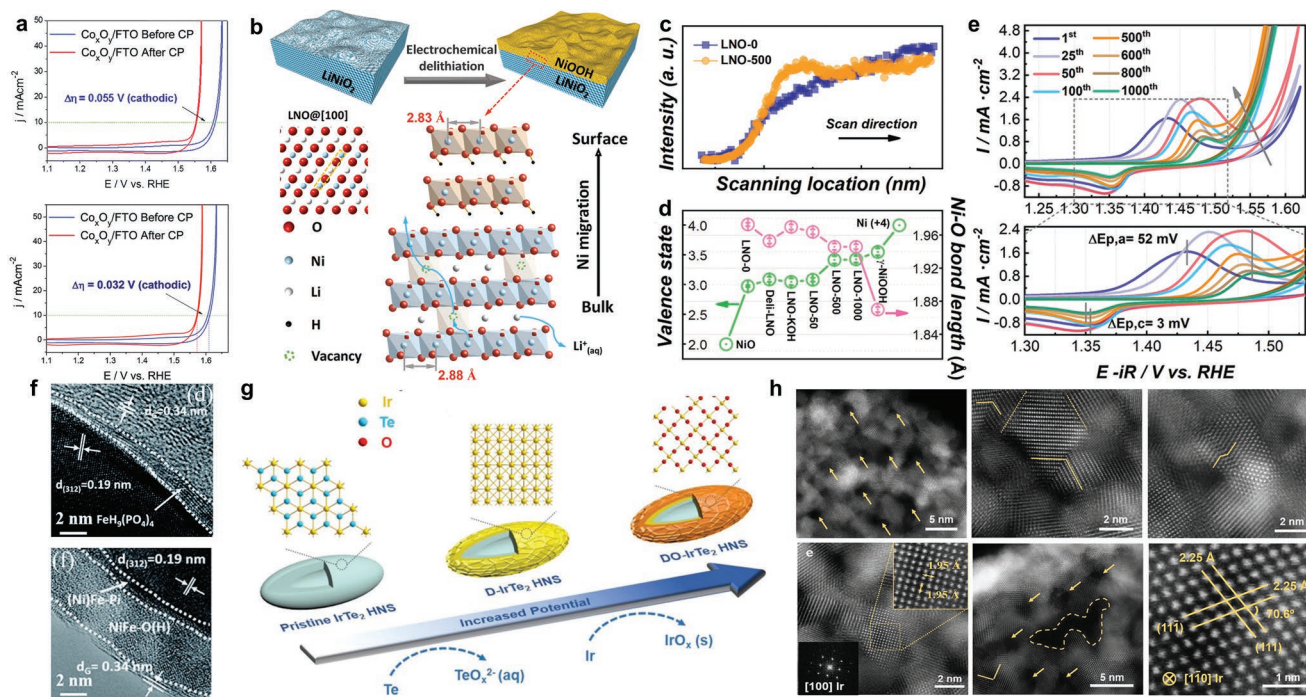


Figure 5. a) CV curves of Co₃O₄/FTO before and after potentiostatic activation (top) and galvanostatic activation (bottom). Reproduced with permission.^[34] Copyright 2017, Royal Society of Chemistry. b) Schematic illustration of the surface reconstruction of LiNiO₂ in the OER process. c) Ni EELS intensity on the near-surface LiNiO₂ before and after activation. d) Valence state and Ni-O bond length of various Ni-based samples. e) CV curves of LiNiO₂ collected at different CV activation cycles. Reproduced with permission.^[53] Copyright 2020, Wiley-VCH. f) HRTEM images of Ni_{1.4}Fe_{0.6}P@rGO after activation cycling (top) and OER process (bottom). Reproduced with permission.^[33] Copyright 2019, Royal Society of Chemistry. g) Schematic illustration of the evolution of IrTe₂ HNS as applied potential increases. h) HRTEM images of D-IrTe₂ HNS (top) and DO-IrTe₂ HNS (bottom). Reproduced with permission.^[54] Copyright 2020, Wiley-VCH.

on the surface of reconstructed catalysts, such as vacancies, grain boundaries, stacking faults and rearrangement of residual atoms (Figure 5h). These defects in DO-IrTe₂ could optimize the local coordination environment and electronic structure of Ir and thus enhance OER catalytic performance. Oh et al. revealed the effect of pH on the reconstruction behavior of IrNi alloy nanoparticles.^[55] In acidic electrolyte, the pre-catalysts would be converted into IrO_x accompanied by Ni leaching upon CV activation, while the Ni-rich IrNiO_x and mildly oxidized IrO_x shell were formed on the surface in alkaline and neutral conditions. In conclusion, the reconstruction behavior can be altered by adjusting electrochemical conditions to yield reconstructed species with the desired structure and catalytic activity.

Naturally, an amorphous shell of active species is formed on the surface of the pre-catalysts to form heterostructures through electrochemical oxidation, which could enable rapid electron transfer at the interface for catalytic reactions. For example, Wang et al. reported that the surface of NiFe and NiCo alloys were transformed into corresponding oxides under galvanostatic electrochemical oxidation (Figure 6a).^[8c] The successful formation of alloy/hydroxide core-shell structures by electrochemical activation of metal alloys could enable higher OER activity of NiFe/NiFe-OH and HER activity of NiCo/NiCo-OH than the parent alloys. In addition, the charge transfer resistance of the heterostructure can be reduced due to the accelerated electron transfer at the interface, which allows for stable water-splitting electrolysis at a large current density of 1 A cm⁻²

for 300 h. Similarly, Zheng et al. have developed nanostructured NiCo alloys with an oxide layer forming through activation of NiCo-SiO₂ composite along with the dissolution of SiO₂ under continuous CV scans.^[56] The presence of the metal core can improve the conductive oxide layer, while the coated oxide layer also contributes to the increased stability.

Activation of metallic compounds such as nitrides, sulfides, and phosphides through the construction of stable metallic oxide on the catalyst surface can also form heterostructures. The formation of reconstructed species on the surface of pre-catalysts can modulate electron structures to accelerate crucial steps in OER reaction. Yang et al. fabricated Co-Ni bimetallic phosphides with a novel 2D/3D structure and confirmed the generation of CoOOH shell on the surface after CV activation,^[59] which could tune the adsorption behavior of OER on the catalyst. Wang et al. proposed an electrochemical surface reconfiguration (ESR) method to construct NiV nitride@oxyhydroxide (NiV@OOH).^[60] The rich NiV/NiVOOH interfaces enlarge the electrochemically active specific surface area and promote the intrinsic OER kinetics. After electrochemical activation, the synergistic effect of metal cations plays an important role in enhancing the activity of reconstructed species. For example, Zou et al. constructed Ni₃Fe_{1-x}V_x/Ni₃Fe_{1-x}V_xN heterojunctions and revealed the formation of NiFeOOH shell on the surface during OER,^[61] in which the variable-valence V^{3+/4+} acted as electron acceptor to boost the electron transfer from the OER intermediates that are adsorbed on the amorphous

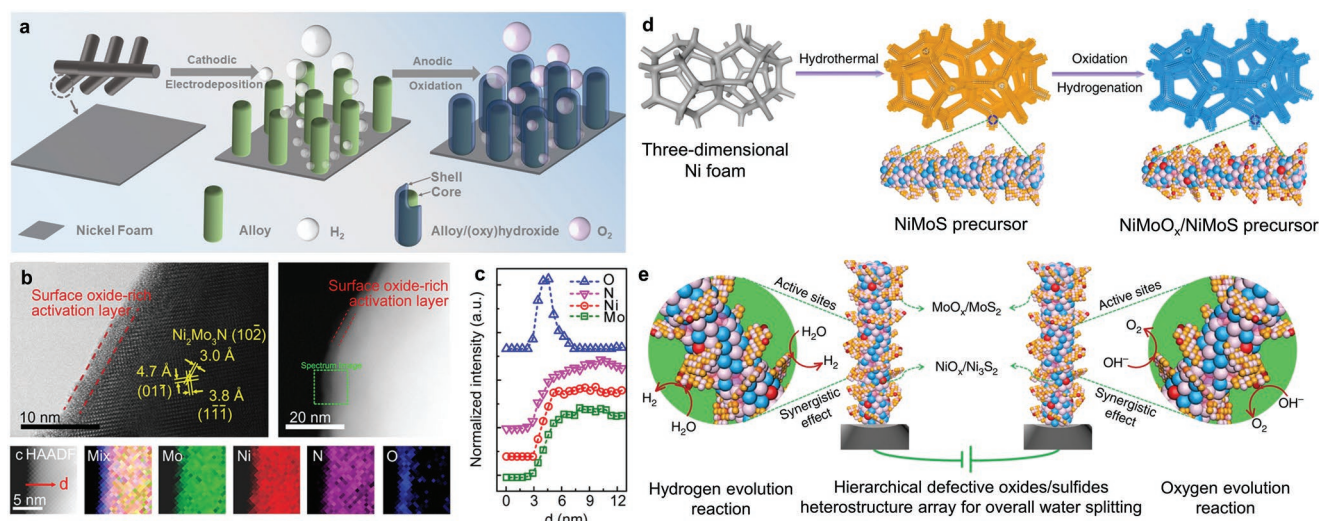


Figure 6. a) Synthetic process of reconstructed NiM/NiM-OH (M = Co and Fe) core-shell catalysts. Reproduced with permission.^[8c] Copyright 2020, Elsevier. b) HRTEM with corresponding EELS mapping images of Ni₂Mo₃N after the OER. c) EELS line scans of oxide-rich activation layer on the surface of Ni₂Mo₃N after the OER. Reproduced with permission.^[57] Copyright 2020, Wiley-VCH. d) Schematic diagram of the preparation and e) catalytic mechanism of NiMoO_x/NiMoS heterostructure. Reproduced with permission.^[58] Copyright 2020, Springer Nature.

NiFeOOH shell. Yang et al. reported that an activation layer with rich oxygen atoms could be formed on the surface of Ni₂Mo₃N under OER conditions.^[57] The HRTEM images can evidence this result along with EELS mapping after the OER (Figure 6b,c), where an amorphous active layer accompanied with concentrating distribution of O on the surface can be observed. The metallic Mo substitution of Ni atoms in activation layer can serve as “electron pump” to transfer electrons to O atoms, which can significantly reduce the free energy for OH deprotonation reaction and the reaction overpotentials to far below those of pure NiO and Ni₂Mo₃N. In summary, reasonable design of pre-catalysts and optimal conditions for electrochemical activation are necessary for obtaining highly active reconstructed species.

It should be noticed that modification of active species through electrochemical activation may easily cause damage to the nanostructure due to the severe dissolution of pre-catalysts. Although increment in material disorder can be achieved due to partial dissolution of specific components, electrochemical activation could also lead to active material loss and decline in the stability of catalysts. Thus, it is extremely challenging to generate highly active while stable catalysts by nondestructive modifications. Zhao et al. immersed La_{0.8}Sr_{0.2}Co_{0.8}Fe_{0.2}O_{3-δ} in an aqueous solution of NaBH₄ at room temperature to form an amorphous layer with abundant oxygen vacancies on the surface accompanied by reduction of Co³⁺ to Co²⁺ and obtained a low overpotential of 248 mV at 10 mA cm⁻².^[62] Plasma treatment provides an efficient strategy for such purpose under mild conditions.^[63] Ostrikov et al. successfully activated metallic sites in CoFe-PBA using air plasma under low temperature,^[64] leading to enhanced OER performance with structural integrity. The plasma treatment can promote the oxidation of Co sites and introduce M-O bonds in CoFe-PBA framework, which is beneficial for enhancement in OER activity of metal catalytic sites. Rational utilization of oxidizing plasma species could construct surface oxide layer, leading to heterostructure. Hou

et al. used oxygen plasma followed by surface hydrogenation to convert NiMoS nanosheets into NiO_x/Ni₃S₂-MoO_x/MoS₂ heterostructure (Figure 6d),^[58] where the former serves as the OER sites whereas the latter as the HER sites (Figure 6e). The coupling interface could optimize the adsorption of H atoms and oxygen-containing intermediates, resulting in the rapid kinetics of water decomposition and thus improving the catalytic performance. Moreover, plasma activation can optimize the structure of the pre-catalysts and facilitate the surface reconstruction. Wang et al. selectively etched Sn off from the surface of SnCoFe perovskite hydroxide by Ar plasma treatment,^[65] which resulted in exposed active CoFe sites with high surface area that allows transformation to an amorphous surface layer during OER process. Owing to its controlled atmosphere and technological process, the application of plasma activation in promoting reconstruction deserves further development.

4.2. Defect Engineering

The surface defect engineering of pre-catalysts, such as step edges, vacancies, and amorphousness, can regulate the electronic structure and local binding environment of metal sites to facilitate the transfer of electrons and increase adsorption of oxygen-containing intermediates,^[66] which would create favorable conditions for rapid reconstruction. In particular, inherent oxygen vacancies can make it easier to trigger reconstruction during catalytic reactions by increasing the electron density surrounding metal atoms, reducing the oxidation states of metal cations. Recently, Xiao et al. have studied the promoting effect of oxygen vacancies in Co₃O₄ (V_O-Co₃O₄) on reconstruction during the OER process via in situ identification of dynamic behavior.^[35] As shown in Figure 7a, oxygen vacancy can initiate the pre-oxidation of Co²⁺ to Co³⁺ at low potential before the OER proceeds. The in situ XPS (Figure 7b) result reveals that oxygen vacancies increase the content of

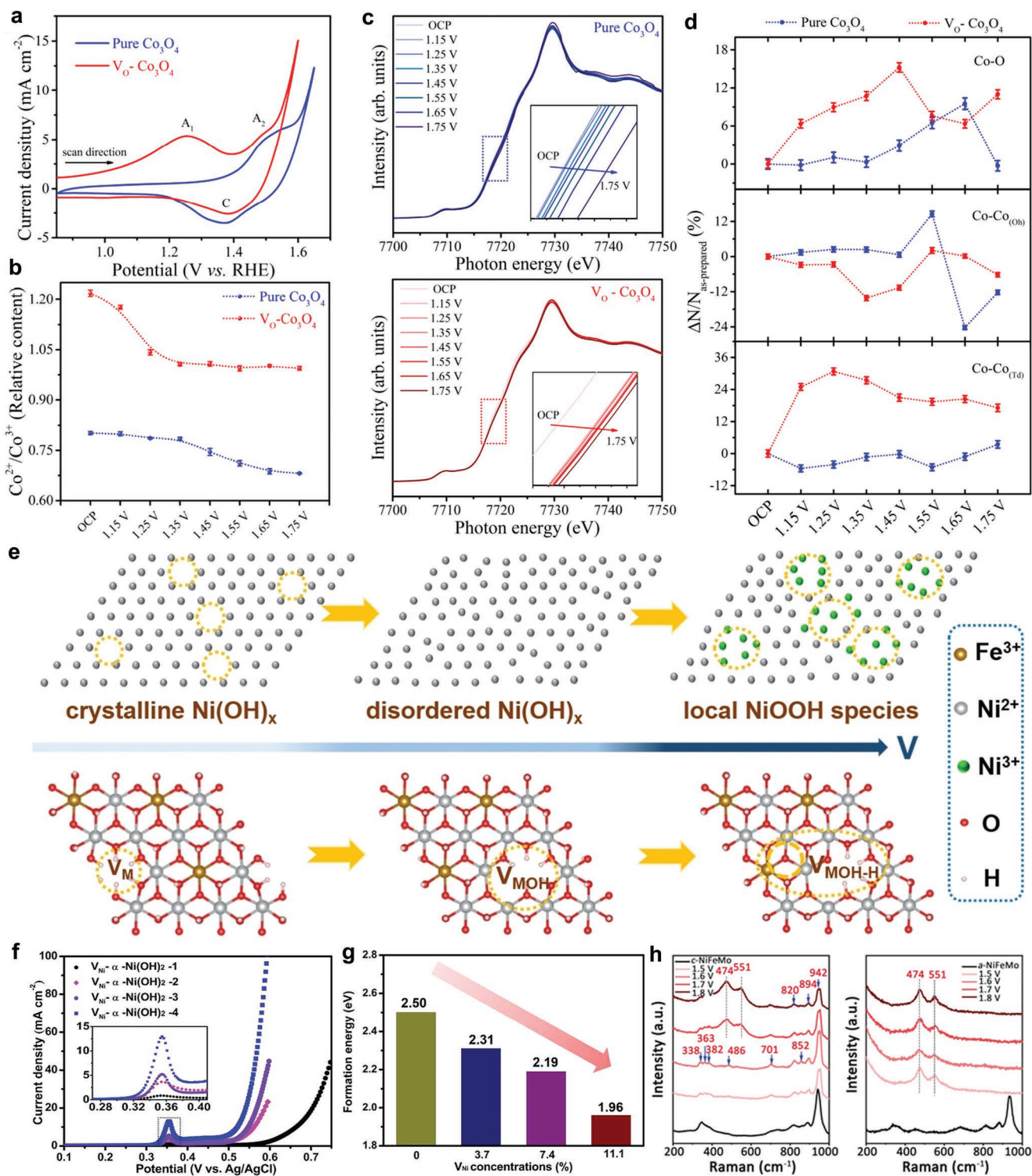


Figure 7. a) The first CV curves of pure Co_3O_4 and $\text{V}_0\text{-Co}_3\text{O}_4$. b) The $\text{Co}^{2+}/\text{Co}^{3+}$ relative content based on the in situ XPS result. c) In situ XANES spectra of pure Co_3O_4 and $\text{V}_0\text{-Co}_3\text{O}_4$. d) The EXAFS coordination number of Co sites with the applied potential. Reproduced with permission.^[35] Copyright 2020, American Chemical Society. e) Evolution of crystalline $\text{Ni}(\text{OH})_x$ species and cationic defects in NiFe-LDH. Reproduced with permission.^[68] Copyright 2021, Wiley-VCH. f) LSV curves of $\alpha\text{-Ni}(\text{OH})_2$ with different concentrations of oxygen vacancies. g) The calculated formation energy of $\gamma\text{-NiOOH}$ with different concentrations of oxygen vacancies. Reproduced with permission.^[69] Copyright 2018, American Chemical Society. h) In situ Raman spectra of $c\text{-NiFeMo}$ and $a\text{-NiFeMo}$. Reproduced with permission.^[70] Copyright 2019, Wiley-VCH.

low-valence Co^{2+} on the surface of $\text{V}_\text{o}\text{-Co}_3\text{O}_4$. Moreover, the $\text{Co}^{2+}/\text{Co}^{3+}$ ratio decreases rapidly with the increase of applied potential, suggesting the occurrence of surface oxidation of $\text{V}_\text{o}\text{-Co}_3\text{O}_4$ at a low potential. In addition, the rapid surface reconstruction can be confirmed by in situ XAS characterization. The large displacement trend observed in Co K-edge XANES spectra (Figure 7c) of $\text{V}_\text{o}\text{-Co}_3\text{O}_4$ suggests the rapid rise of cobalt oxidation state of $\text{V}_\text{o}\text{-Co}_3\text{O}_4$ at low potential, in sharp contrast with the slow shift in the spectra of pure Co_3O_4 . As shown in Figure 7d, the EXAFS coordination number of cobalt ions in $\text{V}_\text{o}\text{-Co}_3\text{O}_4$ begins to decrease at 1.45 V. In comparison, the downshift trend is observed for Co_3O_4 at a higher potential of 1.55 V, which reflects that the Co-OOH^* intermediates on the surface of $\text{V}_\text{o}\text{-Co}_3\text{O}_4$ can achieve deprotonation at a lower potential. Besides, the increasing coordination number of the tetrahedral cobalt sites from open circuit potential state to 1.25 V confirms the rapid combination of OH^- with Co sites during pre-oxidation of Co^{2+} . The promoted effect on the reconstruction may be attributed to the fact that the OH^- in the electrolyte can quickly fill the oxygen vacancies in $\text{V}_\text{o}\text{-Co}_3\text{O}_4$ and combine with Co sites to form active Co-OOH^* intermediates under OER conditions. Zhou et al. synthesized the NiFe LDH electrocatalysts with rich oxygen vacancies ($\text{NiFe-LDH-V}_\text{o}$) by controlling the ratio of $\text{EtOH}/\text{H}_2\text{O}$ in rapid hydrolysis.^[67] The presence of oxygen vacancies can increase the electron density in Ni and Fe d-orbital, resulting in decreased content of electronic spin and unpaired electrons. The enriched electron density on Ni sites would initiate the transition of $\text{Ni}^{2+}/\text{Ni}^{3+}$ at a lower potential, implying the rapid reconstruction under OER conditions. Moreover, the rich oxygen vacancies can facilitate the deprotonation to accelerate the transformation of original n-type $\alpha\text{-NiFe-LDH}$ to active p-type $\gamma\text{-NiFe-LDH}$ on the surface and form p-n junction. The formed p-n junction in NiFe-LDH would regulate OER kinetics due to rapid electron transfer at the interface. The presence of oxygen vacancies not only accelerates the reconstruction reaction, but also reduces the potential required for reconstruction.

Similarly, the cationic vacancies in pre-catalysts can induce surface reconstruction and form more active species during the electrocatalytic process. For example, Zhou et al. revealed that the cationic vacancy defects existing as V_M ($\text{M} = \text{Ni}/\text{Fe}$) in NiFe-LDH could induced the reconstruction of the surface crystalline $\text{Ni}(\text{OH})_x$ to disordered status at low potential and then to local NiOOH species under relatively high voltage.^[68] As shown in Figure 7e, the reconstruction of active species could be attributed to the evolution of cationic vacancy from V_M to $\text{V}_{\text{MOH-H}}$ with increasing voltage. In addition, cationic vacancies can also lead to reduction in the formation energy of reconstructed species. Song et al. revealed that Ni vacancies could optimize the electronic property of $\text{Ni}(\text{OH})_2$,^[69] promoting the formation of active $\gamma\text{-NiOOH}$ species, in agreement with the enlarged oxidation peak of $\alpha\text{-Ni}(\text{OH})_2$ in LSV curves as the concentration of Ni vacancies increases (Figure 7f). Based on the density functional theory (DFT) calculation results, the higher content of Ni vacancies can induce distribution of partial charge density near the Fermi level and reduce the theoretical formation energy of reconstructed $\gamma\text{-NiOOH}$ (Figure 7g). In conclusion, introducing vacancies (both cationic and anionic) in pre-catalysts can enhance the electrochemical activity through structural optimization, thus reducing the energy barrier for formation of reconstructed species.

The transformation of crystalline materials into an amorphous phase proves to be an effective method to improve the degree of defects in the pre-catalysts. The amorphous electrocatalysts possess the advantages of abundant active sites, unsaturated electronic configuration, and structural flexibility, which accelerate the adsorption of reaction intermediates and promote the electron transfer between metal sites and intermediates, thus enabling the rapid reconstruction of the pre-catalysts into active species.^[71] Yu et al. observed the rapid reconstruction occurring on the amorphous NiFeMo oxides ($a\text{-NiFeMo}$).^[70] Based on the in situ Raman spectra (Figure 7h) of $a\text{-NiFeMo}$ and the crystalline counterpart ($c\text{-NiFeMo}$), the pair of peaks at 474 and 551 cm^{-1} are attributed to surface generated NiOOH at a low potential of 1.5 V, meanwhile the characteristic peaks assigned to MoO_3 vanished, suggesting the faster surface evolution of $a\text{-NiFeMo}$ than that of $c\text{-NiFeMo}$, which remains the Mo-O structure at a high potential of 1.8 V. The amorphous structure tends to introduce more vacancies in pre-catalysts during the reconstruction process, which clarifies the origin of the promoted reconstruction and enhanced OER activity.

4.3. Partial Dissolution

Electrocatalysts containing electrochemically unstable species (e.g., perovskites, metal phosphates, and fluorides) would undergo partial dissolution during the OER catalysis, which leads to the reconstruction. In most inorganic ABO_3 or $\text{AB}(\text{OH})_6$ perovskites, the A-site is occupied by alkaline-earth metals and lanthanides, while the B-site is occupied by various transition metals (e.g., Ni, Co, and Ir).^[72] During reconstruction process, A/B-site cationic leaching can induce the formation of unique active species on the surface, such as active hydroxyl groups and reactive oxygen ligands, thereby promoting their OER activity.^[73] Shao et al. selectively etched Sn off of $\text{NiSn}(\text{OH})_6$ perovskite hydroxide to build a Ni^{3+} -containing amorphous layer on the surface,^[74] which facilitates the formation of active metal oxy(hydroxide) species during the OER process. Tileli et al. synthesized $\text{Ba}_{0.5}\text{Sr}_{0.5}\text{Co}_{0.8}\text{Fe}_{0.2}\text{O}_{3-\delta}$ (BSCF) with Co/Fe-rich surface and revealed that the CoFe spinel-like surface was converted into highly active $\text{Co}(\text{Fe})\text{OOH}$ phase,^[75] resulting in enhanced OER electrocatalytic properties. The cationic composition of perovskite can significantly influence the catalytic activity of the reconstructed species. Markovic et al. demonstrated that the content of A-site Sr^{2+} in $\text{La}_{1-x}\text{Sr}_x\text{CoO}_3$ was closely related to the OER activity of formed Co hydr(oxy) oxide (CoO_xH_y) after surface reconstruction.^[76] It was revealed that the generation of more oxygen vacancies in the surface active layer was promoted with the increased Sr doping level in A-site, which induced the enhancement of OER performance. Promoting the reconstruction of perovskites is beneficial for the formation of more active species to improve the OER catalytic performance. Yan et al. proposed a proton-assisted reconstruction to yield highly active reconstructed species.^[77] As illustrated in Figure 8a,b, the A-site cation segregates in typical perovskite oxides including BSCF, $\text{La}_{0.6}\text{Sr}_{0.4}\text{Co}_{0.8}\text{Fe}_{0.2}\text{O}_3$ (LSCF), and $\text{La}_{0.75}\text{Sr}_{0.25}\text{MnO}_3$ (LSM) would be dissolved selectively in an acidic aqueous solution, resulting in the formation

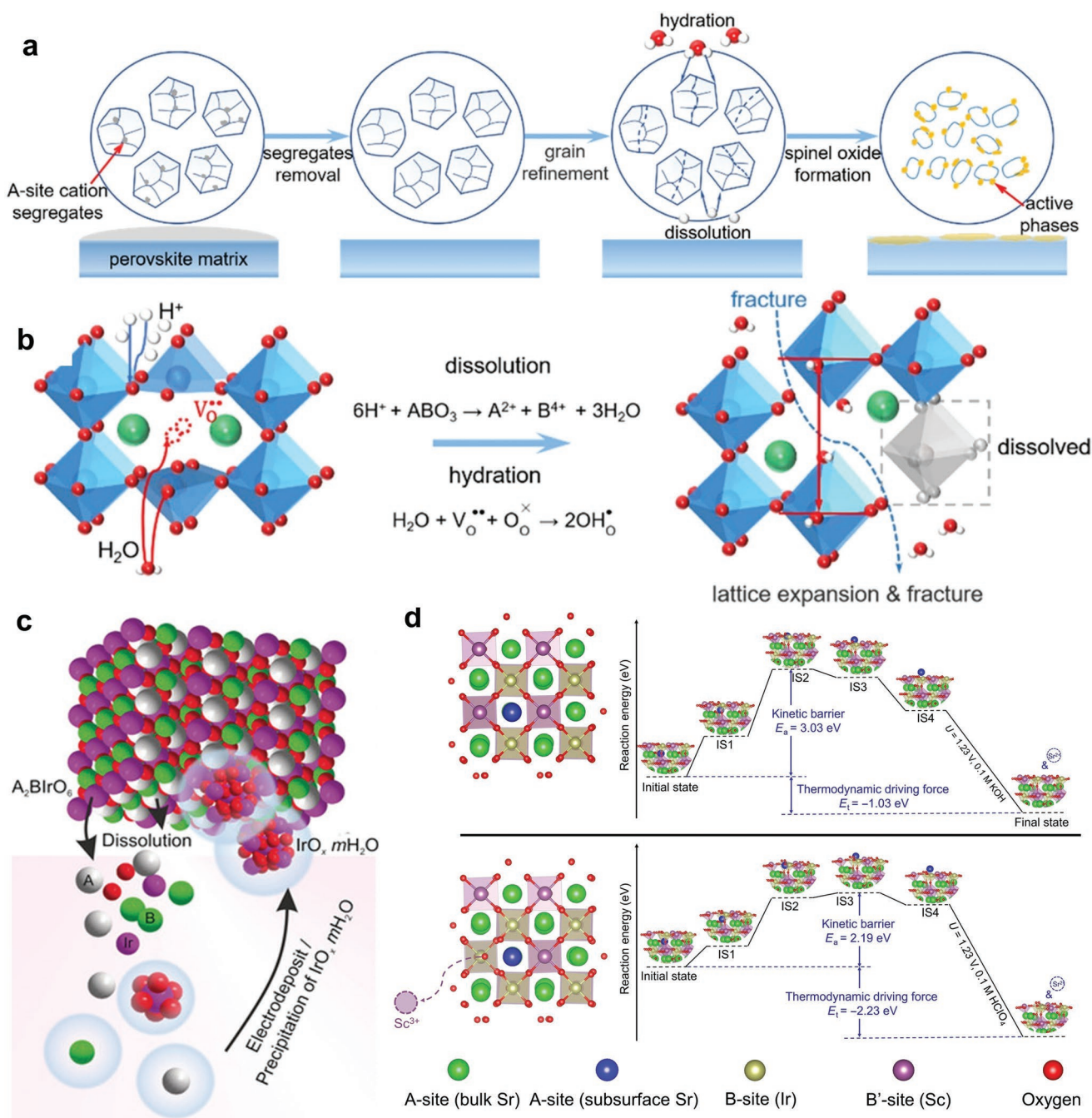


Figure 8. a) Evolution of perovskite oxides by a proton-assisted method. b) Schematic hydration and dissolution of perovskite oxides result in lattice expansion and structural fracture. Reproduced with permission.^[77] Copyright 2021, American Chemical Society. c) Schematic dissolution and precipitation equilibria on the surface of Ir-based perovskites. Reproduced with permission.^[78] Copyright 2019, Wiley-VCH. d) Energy diagrams of the dissolution of A-site (Sr) from the subsurface of $\text{SrSc}_{0.5}\text{Ir}_{0.5}\text{O}_3$ without (top) and with (bottom) a B-site (Sc) vacancy. Reproduced with permission.^[79] Copyright 2021, AAAS.

of spinel oxides on the surface with more active sites exposed. Meanwhile, the protonation via the interaction of oxygen vacancies and H_2O molecules led to the formation of protonic defects and the lattice expansion of the perovskite, resulting in fraction of big particles and generation of small nanoparticles. The reconstructed species exhibited enhanced OER activity as well as excellent stability.

Of note, the surface reconstruction of Ir-based perovskites for acidic OER catalysis have been widely explored. For instance, Kim et al. synthesized Ir oxide black through selective etching of Os oxide in $\text{IrOsO}_x\text{-B}$.^[80] The activated catalyst with large electrochemical active area brings about significantly enhanced OER activity and superior stability. Grimaud et al. revealed the dissolution and precipitation equilibria

on the surface of Ir-based perovskites during the CV activation (Figure 8c).^[78] The deposited $\text{IrO}_x \cdot m\text{H}_2\text{O}$ layer onto the surface of the catalyst is strongly correlated with the OER activity. The properties of the initial bulk phase can greatly affect the reconstruction of Ir-based perovskite and the formation of actual surface active species, including the increase of active sites, the formation and catalytic activity of reactive species as well as the loss of active sites.^[81] Xu et al. studied the role of metal leaching at each geometric site of Ir-based perovskites in reconstruction process.^[79] As displayed in Figure 8d, the activation energy (E_a) for the migration of a lattice Sr from the $\text{SrSc}_{0.5}\text{Ir}_{0.5}\text{O}_3$ without B-site (Sc) defects to the outer electrolyte was higher than that of $\text{SrSc}_{0.5}\text{Ir}_{0.5}\text{O}_3$ with B-site defects, indicating that the thermodynamic stability of B-site cations possessed significant influence on kinetics barriers for reconstruction process. Hence, the order of leaching of A- and B-site cations can be tuned by tailoring the thermodynamic stability of B-site cations. They also found that the dissolution of Sr at A-site mainly enlarged electrochemical surface area for the OER, while additional leaching of Sc from B-site induced the formation of a honeycomb-like IrO_xH_y phase with high intrinsic activity. The effect of cationic composition on the reconstruction of Ir-based perovskites was also confirmed by Xu et al.^[82] They introduced cobalt cations to replace Ir sites in cubic $\text{SrCo}_{0.9}\text{Ir}_{0.1}\text{O}_{3-\delta}$ perovskite and found that the Sr and Co leaching contributed to the thicker reconstructed layers and more oxygen vacancies in the formed IrO_xH_y phase compared with monoclinic SrIrO_3 perovskite, thus resulting in enhanced OER activity. However, severe metal dissolution and surface structural reconstruction during OER would lead to structural collapse and loss of active sites. To solve this problem, Zou et al. synthesized an ultra-thin SrIrO_3 perovskite with exposed (001) facets by template-confined growth method. The high stability of (001) facets inhibited the excessive dissolution of Sr and Ir,^[83] enabling excellent structural stability during acidic OER process. In order to design perovskite oxides as pre-catalysts with predictable and controllable reconstruction behavior, it is necessary to further explore the fundamental relationship of the composition and structure of the initial bulk phase and the surface evolution process.

For other non-perovskite catalysts, the reconstruction of pre-catalysts can be also triggered by partial dissolution of less stable components under electrochemical conditions,^[49,62,84] enabling more metal atoms in pre-catalysts to be exposed or converted into catalytically active sites at low overpotentials. For example, Zhang et al. demonstrated that partial dissolution of Fe metal atoms in FeNi alloy fiber paper exposes more Ni atoms under electrochemical oxidation,^[36] which can be further oxidized by the residual Fe^{3+} ions to form an active NiFeOOH layer. The presence of Fe in the oxyhydroxide layer on $\text{Ni}_{0.6}\text{Fe}_{0.4}$ alloy paper can elongate the bond length of Ni-O, which contributes to reducing the energy barrier for dissociation of oxygen-containing intermediates on active sites. Li et al. prepared a unique glass-ceramic catalyst ($\text{Ni}_{1.5}\text{Sn}@ \text{triMPO}_4$) by coupling crystalline $\text{Ni}_{1.5}\text{Sn}$ nanoparticles with ternary NiFeSn phosphate (triMPO_4) and found easier dissolution of Sn^{4+} from $\text{Ni}_{1.5}\text{Sn}@ \text{triMPO}_4$ that facilitates the surface reconstruction during electrochemical activation,^[85] leading to the formation of NiFeOOH with rich defects (Figure 9a). The rapid structural evolution may be assigned to the lower vacancy formation energy of Sn^{4+}

in $\text{Ni}_{1.5}\text{Sn}@ \text{triMPO}_4$ compared with that in triMPO_4 , meaning that Sn^{4+} can be dissolve easily from glass-ceramic structure to expose Ni and Fe species to the electrolyte for further oxidation. Besides, the highest adsorption energy of PO_4^{3-} on oxygen vacancy sites also plays a crucial role in accelerating the surface reconstruction. The active NiOOH layer with intrinsic oxygen vacancy and remaining PO_4^{3-} formed on the surface of $\text{Ni}_{1.5}\text{Sn}@ \text{triMPO}_4$ accounts for the higher OER activity. Li's group reported that the $\text{Ni(Fe)O}_x\text{F}_y$ nanosheets (F-NiFe) prepared by fluorination-enabled reconstruction of NiFe metal nanoparticles (NiFe) could be transformed into Fe-enriched $\text{Ni(Fe)O}_x\text{H}_y$ through in situ electrochemical activation.^[86] The F dopants can accelerate the formation of reconstructed $\text{Ni(Fe)O}_x\text{H}_y$ because the fluorine is easily leached off. As shown in Figure 9b, the OER currents and Ni redox peak area of F-NiFe increase more rapidly than NiFe upon continuous activation cycles. The surface evolution of the two NiFe-based pre-catalysts was investigated by operando Raman analysis (Figure 9c), which shows that the peak intensity of F-NiFe is higher than that of NiFe at the same reaction time. Besides, the F-NiFe after activation (F-NiFe-A) possesses a thicker reconstructed layer than NiFe-A due to F dopants' modification. These results validate that the F dopants introduced by fluorination can significantly enhance the degree of in situ surface reconstruction of $\text{Ni(Fe)O}_x\text{F}_y$ in electrochemical activation. Furthermore, the deep surface reconstructed layers account for the increased OER activity as well. Hence, doping pre-catalysts with soluble species is an effective way to promote the reconstruction process through partial dissolution.

It can be observed in perovskites as discussed earlier that the partial dissolution of pre-catalysts during the reconstruction process would also introduce oxygen vacancies to the newly formed species,^[77,82] resulting in enhanced catalytic activity. The phenomenon also exists in other non-perovskite catalysts. Chen et al. presented a novel method to facilitate the surface reconstruction of amorphous FeB via W-P co-doping to optimize the alkaline OER activity.^[90] During the OER process, the formation of W-doped iron oxyhydroxides (W-FeOOH) on the surface of catalysts is accelerated by the etching of B and P components, leading to the exposure of abundant coordinatively active sites. The dissolution of B and P also resulted in more oxygen vacancies that tune the surface electron properties of reconstructed W-FeOOH . In addition, the promoting surface construction of CoCr_2O_4 can be achieved via the leaching of Cr accompanied by the depletion of lattice oxygen.^[87] The O 1s XPS characterizations (Figure 9d) indicate the consumption of lattice oxygen during the OER process due to the formation and dissolution of $(\text{CrO}_4)^{2-}$ at high potentials, which creates oxygen vacancies that further accelerate the oxidation of Co species, in agreement with the positive shift of Co K-edge XANES spectra (Figure 9e). The Co K-edge FT-EXAFS spectra confirm the formation of CoO_6 octahedra on the surface. As shown in the scheme of surface evolution in pristine CoCr_2O_4 (pri- CoCr_2O_4) during surface oxidation (Figure 9f), the Cr leaching would start at a low potential accompanied with the transition of $\text{Cr}^{3+}/\text{Cr}^{4+}$, and then get oxidized to $(\text{CrO}_4)^{2-}$ with the loss of lattice oxygen. This would induce the transformation of tetrahedral Co cation ($\text{Co}^{2+\text{Td}}$) into octahedral Co ($\text{Co}^{3+/4+\text{Oh}}$) through a non-concerted proton-electron transfer, and the construction of amorphous

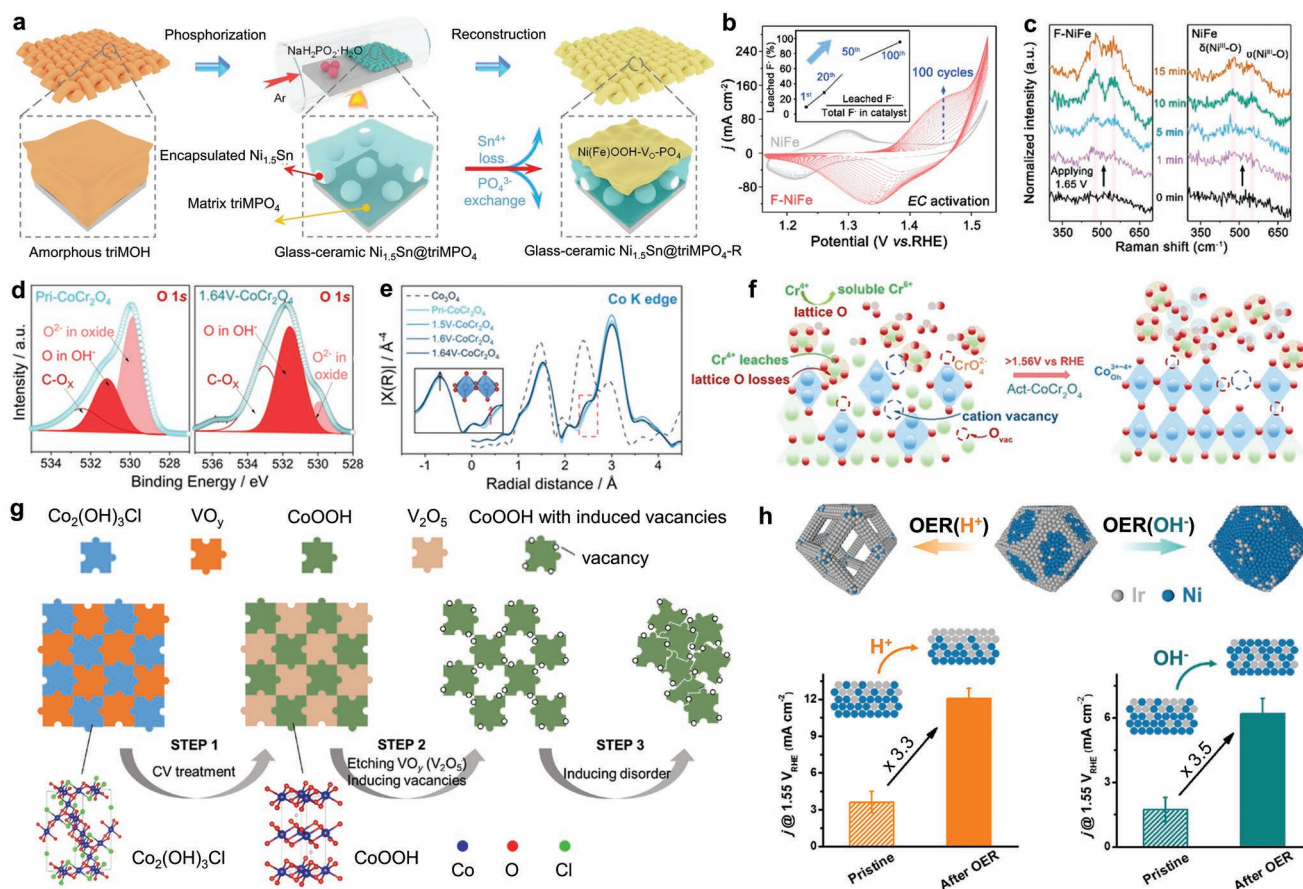


Figure 9. a) Synthetic process of $\text{Ni}_{1.5}\text{Sn}@ \text{triMPO}_4$ followed by surface reconstruction. Reproduced with permission.^[85] Copyright 2021, Wiley-VCH. b) CV curves of F-NiFe and NiFe electrocatalysts collected at different CV activation cycles (inset: percentage of leached F⁻ in the total amount of F in F-NiFe). c) In situ Raman spectra of F-NiFe and NiFe electrocatalysts. Reproduced with permission.^[86] Copyright 2021, American Chemical Society. d) O 1s XPS and e) Co K-edge XANES spectra of $\text{pri-CoCr}_2\text{O}_4$ and CoCr_2O_4 activated at a different potential. f) Schematic reconstruction of CoCr_2O_4 . Reproduced with permission.^[87] Copyright 2021, Wiley-VCH. g) Schematic structural evolution for $\text{Co}_2(\text{OH})_3\text{Cl}/\text{VO}_y$ during reconstruction. Reproduced with permission.^[88] Copyright 2020, Wiley-VCH. h) The schematic reconstruction process of IrNi_x nanoparticles along with the promoted effect on OER activity in acidic and alkaline solution. Reproduced with permission.^[89] Copyright 2018, American Chemical Society.

oxyhydroxide layer with a large number of oxygen vacancies in the CoCr_2O_4 after activation ($\text{act-CoCr}_2\text{O}_4$). Fan et al. proposed an effective method to modify oxygen vacancies in reconstructed CoOOH by selectively etching vanadium oxides (VO_y) in $\text{Co}_2(\text{OH})_3\text{Cl}/\text{VO}_y$ through CV treatment to eliminate some O atoms near Co sites.^[88] As illustrated in Figure 9g, the formed CoOOH layer with high content of oxygen vacancies is transformed into a disordered structure, resulting in abundant Co active sites exposed for better OER activity. The content of oxygen vacancies in reconstructed CoOOH has been demonstrated to be positively correlated with the introduced content of VO_y in pre-catalysts. Reasonable content of oxygen vacancies is favorable for enhancement in OER activity of obtained CoOOH .

In a particular situation, the leaching of components in catalysts induced by reconstruction will cause the migration of cations and form active layer on the surface. Jiang et al. demonstrated that the Fe in the inner shell of Cu@Fe@Ni three-layer heterostructure would migrate into Ni shell to generate Fe-doped NiOOH active species during the reconstruction process.^[91] Huang et al. revealed the dynamic migration process of Ni in IrNi_2 nanoparticles during electrochemical oxidation in

acidic and alkaline solutions.^[89] As shown in Figure 9h, the Ni atoms migrate from the inner structure to the surface, where they are oxidized to Ni oxides during the alkaline OER process. In acidic conditions, the presence of H⁺ would facilitate the Ni migration and lead to the dissolution of Ni species, resulting in the formation of Ir framework containing a few Ni dopants. Subsequent electrochemical tests showed that the structural evolution of IrNi_2 induced by Ni migration enhances both the acidic and alkaline OER performance.

In addition, partial dissolution of atoms in pre-catalysts can introduce relevant heteroatoms into active species, forming a highly amorphous active layer with a well-modulated electronic structure and abundant defects. For example, in situ surface reconstruction of Ni_5P_4 pre-catalyst rendered P-doping NiO with high electrocatalytic activity.^[92] After OER catalysis, a small amount of P-O existed in the reconstructed NiO shell, although most of P are oxidized and leached into electrolyte. The doping of P in newly formed NiO can effectively lower the d-band position, suggesting reduced binding strength of OER intermediates. Similarly, Zhao et al. reported an active V-doped NiOOH with a highly disordered structure obtained by partial etching

of V in V-doped Ni_2P pre-catalysts under electrochemical oxidation.^[93] The V dopants could lower Ni valence state and optimize the local bonding environment of V- Ni_2P /NF-AC, contributing to higher OER performance.

In conclusion, the partial dissolution of pre-catalysts during electrochemical reconstruction affects the surface restructuring behavior and catalytic activity of newly formed species. Therefore, electrochemically unstable components can be appropriately introduced into pre-catalysts to achieve the effective reconstruction. However, the ion leaching might also destroy the crystal structure of electrocatalysts, especially in alkaline OER environments. Ensuring the stability of crystal matrix structure while triggering ion leaching has become a hot research topic.

4.4. Ionic Doping

The incorporation of ions into the pre-catalysts can optimize the electronic structure and regulate dynamic restructuring of pre-catalysts.^[94] Reconstruction of pre-catalysts can be induced by metal or non-metal heteroatom doping, which can trigger the reorganization of the atomic arrangement.^[62,95] For example, Wang et al. prepared Ru- $\text{RuP}_x\text{-Co}_x\text{P}$ with promoted OER performance via the surface reconstruction of Co_2P induced by the in situ doping of Ru.^[96] The in situ doping of Ru into Co_xP can decrease the Gibbs free energy for the transition of O^* to OOH^* and increase the projected density of states on the active sites of catalysts in the catalytic reaction. Incorporation of heteroatoms into pre-catalysts can also enhance the intrinsic conductivity and regulate the electronic structure

of reactive species, offering favorable triggering condition for surface reconstruction. Not only that, the dopants remaining in reconstructed species also could enhance the catalytic activity. In particular, the strong electronegativity of F anions as dopants can form weak metal-fluorine chemical bonds, which are easily broken and transformed into F doping metal (oxy)hydroxides during the reconstruction process. The F dopants can also tune metal sites' electronic structure and adsorption energy to boost catalytic activity.^[97] Ma et al. reported a fluorination strategy of NiFe Prussian blue analogue (NiFe-PBAs) to replace CN^- ligand with F^- anions and the fluoride product (NiFe-PBAs-F) would be converted into F-doped NiFeOOH due to the migration of F during electrochemical reconstruction.^[98] Similarly, Ju et al. revealed that the formation of F-doped CoOOH nanosheets could be promoted by F migration during electrochemical oxidation of CoF_2 nanowires.^[99] The accumulation of F dopants on the surface enables the hydrophilic surface to accelerate the adsorption of oxygen-containing intermediates, thus boosting the OER performance.

Similarly, the chloride ion can also act as dopants to regulate the structure of the pre-catalyst, boosting the reconstruction reaction. Lim et al. doped chlorine into LiCoO_2 pre-catalyst ($\text{LiCoO}_{1.8}\text{Cl}_{0.2}$) to conduct fast phase transition into active amorphous oxyhydroxide, accompanied by cobalt electrochemical oxidation and Li^+ leaching.^[100] As shown in Figure 10a, the normalized Co K-edge XANES spectra for $\text{LiCoO}_{2-x}\text{Cl}_x$ shift to lower energy region as the Cl content increases, which demonstrates reduction of the valence state of Co due to the replacement of O^{2-} with Cl^- . The Co^{2+} in $\text{LiCoO}_{1.8}\text{Cl}_{0.2}$ would be oxidized to Co^{3+} at a lower positive potential, which could initiate the reconstruction of $\text{LiCoO}_{1.8}\text{Cl}_{0.2}$ below 1.4 V. For comparison, the

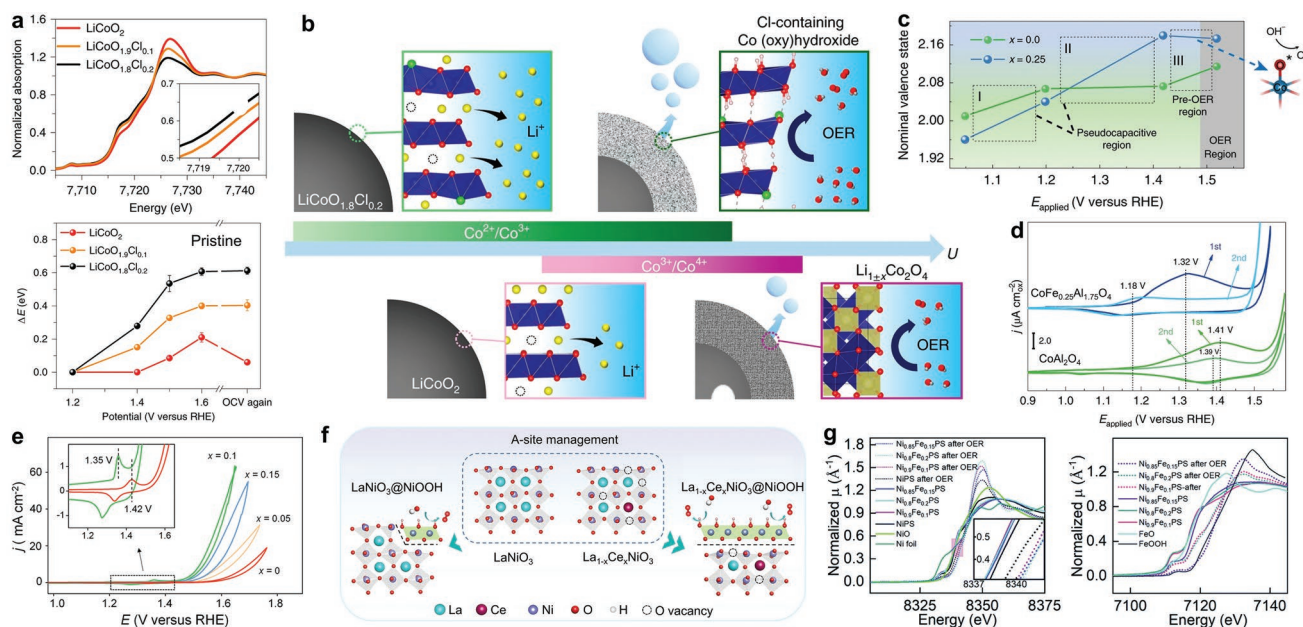


Figure 10. a) Co-K edge XANES spectra recorded at OCV (top) and their shift recorded at different potential for $\text{LiCoO}_{2-x}\text{Cl}_x$ ($x = 0, 0.1$ or 0.2) (bottom). b) Schematic mechanism of delithium process for $\text{LiCoO}_{1.8}\text{Cl}_{0.2}$. Reproduced with permission.^[100] Copyright 2021, Springer Nature. c) Cobalt valence state obtained at different potential and d) CV curves of $\text{CoFe}_{0.25}\text{Al}_{1.75}\text{O}_4$ and CoAl_2O_4 . Reproduced with permission.^[101] Copyright 2019, Springer Nature. e) CV curves of $\text{La}_{1-x}\text{Ce}_x\text{NiO}_3$ ($x = 0, 0.05, 0.1$ and 0.15). f) Schematic surface reconstruction process of $\text{La}_{1-x}\text{Ce}_x\text{NiO}_3$ to NiOOH. Reproduced with permission.^[102] Copyright 2021, Wiley-VCH. g) Ni and Fe K-edge XANES spectra for $\text{Ni}_{1-x}\text{Fe}_x\text{PS}$ ($x = 0.1, 0.15$ or 0.2) before and after the OER. Reproduced with permission.^[103] Copyright 2020, Royal Society of Chemistry.

reconstruction of LiCoO_2 started after 1.4 V due to the sole transition of $\text{Co}^{3+}/\text{Co}^{4+}$ during OER process. In addition, the early reconstruction induced by Cl dopants can initiate delithium at a lower positive potential. It can be noted in Figure 10b that $\text{LiCoO}_{2-x}\text{Cl}_x$ is transformed into Cl-containing cobalt oxyhydroxide with superior OER activity at much lower delithium potentials, in sharp contrast to Cl-free LiCoO_2 , which is transformed into less active $\text{Li}_{1-x}\text{Co}_2\text{O}_4$.

Certain ions can initiate the surface reconstruction of pre-catalysts at a lower potential for fast formation of active phase by modulating electronic structure or creating rich vacancies. For example, Xu et al. revealed that the Fe dopants could facilitate surface reconstruction of CoAl_2O_4 at low potentials.^[101] Figure 10c shows a continuous increase in the cobalt valence based on in situ XANES spectra for $\text{CoFe}_{0.25}\text{Al}_{1.75}\text{O}_4$ in the range of 1.05–1.44 V. In comparison, the increment in cobalt valence for CoAl_2O_4 is observed only in 1.05–1.2 V and 1.42–1.52 V regions, implying the positive effect of Fe substitution on the cobalt oxidation. The cobalt pre-oxidation of $\text{CoFe}_{0.25}\text{Al}_{1.75}\text{O}_4$ would be triggered at low potential with a clear anodic peak at 1.32 V (Figure 10d) due to the fast surface reconstruction promoted by Fe substitution, while Co pre-oxidation of CoAl_2O_4 located at 1.41 V. In addition, the appropriate Fe substitution would upshift the O 2p level to be close to the Fermi level, which contributes to the lattice oxygen oxidation for OER occurring at low potential. In addition, Sun et al. disclosed that the Ce doping in perovskite LaNiO_3 could significantly reduce the required potential for reconstruction of Ni sites (Figure 10e).^[102] Furthermore, the reconstruction onset potential of $\text{La}_{1-x}\text{Ce}_x\text{NiO}_3$ gradually decreases with the increasing of Ce content. The Ce dopants can upshift the Ni 3d and O 2p band center, which is conducive to the appearance of oxygen vacancies in $\text{La}_{1-x}\text{Ce}_x\text{NiO}_3$. As displayed in Figure 10f, the abundant oxygen vacancies formed by Ce doping would facilitate the surface reconstruction and formation of active phase, which could explain the superior OER performance of $\text{La}_{1-x}\text{Ce}_x\text{NiO}_3$.

The dopants can facilitate electron transfer between atoms and regulate the electronic distribution in pre-catalysts, which would change the valence state of metal sites and exert a significant influence on the reconstruction kinetics. Zeng et al. have found that the regulation of P dopants in $\text{Co}(\text{SeP})_2$ would reduce cobalt valence states,^[104] which remarkably regulates the restructuring kinetics for accelerating the nucleophilic reaction with OH^- to create more CoOOH . The P substitution was found to increase the ratio of $\text{Co}^{3+}/\text{Co}^{2+}$ in $\text{Co}(\text{SeP})_2$ after electrochemical activation, indicating that the P dopants promote the formation of CoOOH . Similarly, the higher content of P could also motivate the generation of oxygen vacancies, which benefit the adsorption and dissociation of H_2O . Certain dopants can not only promote the reconstruction process but also enhance the catalytic activity of the newly formed species.^[105] Peng et al. found that moderate Fe doping in NiPS could modify the oxidation state of Ni to improve catalytic efficiency after the surface reconstruction.^[103] As shown in the Ni K-edge XANES spectra (Figure 10g), the Ni on the surface of $\text{Ni}_{0.85}\text{Fe}_{0.15}\text{PS}$ exhibits the lowest oxidization state due to the electron transfer from Fe to Ni, in accordance with the positive shift of $\text{Ni}_{0.85}\text{Fe}_{0.15}\text{PS}$ in Fe K-edge XANES spectra. In addition, the highest valence state of Ni and Fe also could be observed in $\text{Ni}_{0.85}\text{Fe}_{0.15}\text{PS}$ after OER,

suggesting that the appropriate Fe regulation is beneficial to the formation of metal oxyhydroxide with high valence state, which can increase the adsorption strengths for oxygen-containing intermediates during OER. Sun et al. revealed that Mo substitution can serve as electron donor to stabilize metastable hexagonal close-packed metallic cobalt phase in polymorphic cobalt oxides,^[106] which would undergo fast surface reconstruction to generate stabilized $\text{Co}^{3+}/\text{Co}^{2+}$ active centers accompanied by excellent catalysis (onset overpotential of 210 mV and overpotential at 10 mA cm^{-2} of 290 mV), proving key role of surface reconstruction kinetics in electrochemical catalytic activity. As a result, the reconstruction behavior is correlated to the structural properties of the pre-catalysts, which can be optimized by ionic doping.

4.5. Heterostructure Construction

Improving structural property through designing heterostructure by the combination of two or more dissimilar materials to achieve mutual advantages has also been regarded as an effective strategy to boost the reconstruction process.^[107] The new component introduced in heterostructure can support the reconstruction of pre-catalysts to form abundant active species for raised catalytic performance. For example, Hou et al. revealed that coupling of Ir clusters with amorphous CoNiB induced the formation of high-valence cobalt species on the surface.^[108] The Ir–O–Co bridges between iridium and the formed oxyhydroxides allowed effective proton-electron transfer to trigger multiple active sites for high intrinsic OER activity. Yan et al. synthesized BaIrO_3 covered with highly active 1 nm IrO_x particles ($\text{IrO}_x/\text{BaIrO}_3$) by solution calcination followed by treatment using strong acids.^[109] As shown in the high-angle annular dark field scanning TEM (HAADF-STEM) images (Figure 11a), the IrO_x nanoparticles on the surface were evolved into thicker amorphous layer during the acidic OER, while the 9R- BaIrO_3 layer with face-sharing IrO_6 trimer structure was transformed into IrO_6 octahedron structures accompanied with Ba leaching. In addition, the shift of Ir $4f_{7/2}$ peak in Ir 4f XPS (Figure 11b) spectra indicating that the Ir^{4+} species existed in the initially formed amorphous layer after 50 cycles and evolved into Ir^{5+} species after 5000 cycles, while the O K-edge XANES spectra confirmed the existence of Ir–O covalency in formed amorphous layer. These results suggested that the initial IrO_x nanoparticles/ BaIrO_3 heterostructure was transformed into amorphous $\text{Ir}^{4+}\text{O}_x\text{H}_y/\text{IrO}_6$ octahedrons and then to amorphous $\text{Ir}^{5+}\text{O}_x/\text{IrO}_6$ octahedrons on the surface, which was responsible for the excellent acidic OER activity.

The interfaces of heterostructure could accelerate the electron transfer due to the difference in electronegativity between two components, effectively modulating active species' electronic structure.^[113] Therefore, the reactive species can be supported by counterparts with high electrical conductivity to tune its electron distribution and facilitate the adsorption/desorption of intermediates on the surface, resulting in an enhancement in catalytic kinetics. Gao et al. reported pre-catalysts based on the core-shell $\text{Ni}_3\text{N}/\text{Ni}@ \text{Ni}_3\text{N}$ with excellent OER activity prepared by thermal nitridation method.^[114] In this heterostructure, the electrons flow from highly conductive Ni atoms to

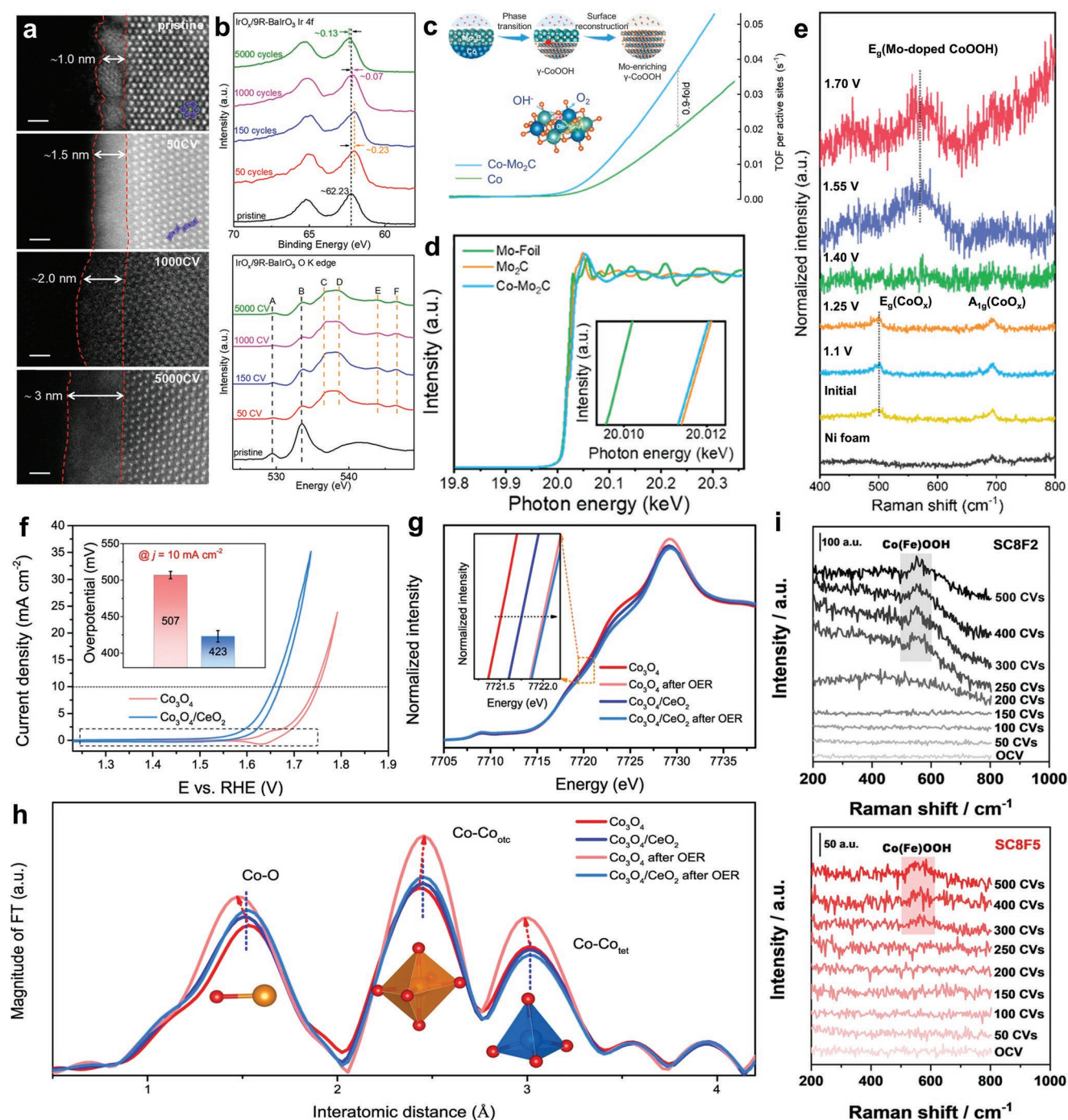


Figure 11. a) Lattice-resolved HAADF-STEM images and b) Ir 4f XPS spectra (up) and O K-edge XANES spectra (bottom) of IrO_x/BaIrO₃ after different CV cycles. Reproduced with permission.^[109] Copyright 2021, American Chemical Society. c) Schematic reconstruction process of Co-Mo₂C to Mo-rich γ -CoOOH and TOF curves before and after reconstruction. d) Mo K-edge XANES spectra of Mo-foil, Mo₂C, and Co-Mo₂C. e) In situ Raman spectra of Co-Mo₂C. Reproduced with permission.^[110] Copyright 2020, American Chemical Society. f) CV curves of Co₃O₄ and Co₃O₄/CeO₂. g) Co K-edge XANES and h) Co K-edge EXAFS spectra of Co₃O₄ and Co₃O₄/CeO₂ before and after the OER. Reproduced with permission.^[111] Copyright 2021, Springer Nature. i) In situ Raman spectra of SC8F2 and SC8F5. Reproduced with permission.^[112] Copyright 2021, American Chemical Society.

Ni₃N, which modifies the electron density on the surface to promote the surface reconstruction of Ni₃N/Ni@Ni₃N, generating NiOOH layers and creating new heterostructures in the form of Ni@NiOOH and Ni₃N@NiOOH with rich interface sites. The electrons flow from NiOOH to Ni₃N, generating positively

charged surface of NiOOH that favors the adsorption of OER intermediates. In addition, rationally constructing the heterostructure with strong interfacial electronic interactions can modify the electronic structure of reactive species and expose more active sites in pre-catalysts to facilitate reconstruction during

the catalytic reaction. Guo et al. demonstrated the positive effect of interfacial electronic features on surface construction for CoFe_2O_4 coupling with $\text{Co}_3(\text{PO}_4)_2$ (CoPi).^[115] The electron transfer from CoFe_2O_4 to CoPi leaves holes in CoFe_2O_4 -CoPi heterostructure with increased density of state near E_F . The change in electron distribution could benefit the transformation of Co sites combined with adsorbed OH^- into Co oxyhydroxide. Kou et al. synthesized a Co-based heterostructure composed of Co metal and Mo_2C components (Co- Mo_2C), which could undergo a fast transformation of metallic Co into $\gamma\text{-CoOOH}$ and doping of Mo into $\gamma\text{-CoOOH}$ during the OER, for increasing turnover frequency (TOF) (Figure 11c).^[110] The Mo K-edge XANES spectrum of Co- Mo_2C presents an adsorption edge energy lower than that of Mo_2C (Figure 11d), indicating electron transfer from Co to Mo_2C in the heterostructure, which would reduce required energy for the formation of $\gamma\text{-CoOOH}$. The in situ Raman spectroscopy was performed to observe the phase transition and Mo-enriched surface reconstruction. As shown in Figure 11e, the broad band assigned to $\gamma\text{-CoOOH}$ in Raman spectra appears at 1.4 V and further strengthens with the potential increase. The strong π -donation is the dominant interaction between O^{2-} and Co^{3+} in the presence of e^- - e^- repulsion connecting Mo^{4+} and bridging O^{2-} in reconstructed Mo-doped $\gamma\text{-CoOOH}$, which increases the electron density of Co species and reduces the free energy for desorption of oxygen-containing intermediates on Co sites. In conclusion, the construction of heterostructure in pre-catalysts remarkably promote the electron transfer for reconstruction reaction and thus the OER catalysis.

The local bonding environment surrounding the metal center in catalysts can be regulated by interface effect, facilitating conversion of active species during surface reconstruction. Huang et al. coupled Co_3O_4 with CeO_2 to form $\text{Co}_3\text{O}_4/\text{CeO}_2$ heterostructure for acidic OER and found that the redox properties of $\text{Co}_3\text{O}_4/\text{CeO}_2$ are changed in the presence of CeO_2 .^[111] As shown in Figure 11f, there is no redox peak attributed to transition of dimeric Co(III)Co(IV) to Co(IV)Co(IV) in the CV curve of $\text{Co}_3\text{O}_4/\text{CeO}_2$ at high potential, implying the fast formation of Co(IV) active species without combination with each other to form dimeric Co(IV)Co(IV) . As displayed in Figure 11g, the negative shift of Co K-edge XANES spectra of Co_3O_4 after coupling with CeO_2 indicates increased Co oxidation valence in heterostructure owing to the electron transfer from Co_3O_4 to CeO_2 . Importantly, the variations of local bonding for $\text{Co}_3\text{O}_4/\text{CeO}_2$ can be reflected by the Co K-edge EXAFS (Figure 11h), which exhibits shorter bonds of Co-O and Co- Co_{oct} (octahedral Co cation) and longer bonds of Co- Co_{tet} (tetrahedral Co cation) in $\text{Co}_3\text{O}_4/\text{CeO}_2$, suggesting electronic redistribution induced by CeO_2 . The modified local bonding environment via the introduction of CeO_2 can initiate the translation of Co sites to Co (IV) at a lower potential, thereby avoiding the charge accumulation under the OER process at large potential, which enables rich active Co (IV) with enhanced catalytic activity.

It should be noted that uncontrolled reconstruction may lead to the excessive dissolution of metallic cations and collapsed structure of pre-catalyst, resulting in decreased activity and poor stability. Fortunately, the ruinous effect of reconstruction could be restrained by the introduction of robust components as a stable phase to interact with the active phase. Yi et al.

reported the $\text{SrCo}_{0.8}\text{Fe}_{0.5-x}\text{O}_{3-\delta}/\text{Fe}_x\text{O}_y$ (SC8F5) heterostructure by segregating Fe_xO_y phase from single-phase $\text{SrCo}_{0.8}\text{Fe}_{0.5}\text{O}_{3-\delta}$ via a thermal-induced phase-segregation method.^[112] After coupling with Fe_xO_y , the SC8F5 exhibits higher stability than $\text{SrCo}_{0.8}\text{O}_{3-\delta}$ (SC) and $\text{SrCo}_{0.8}\text{Fe}_{0.2}\text{O}_{3-\delta}$ (SC8F2) during the long-term OER process due to the slight leaching of Sr in the presence of Fe_xO_y . Besides, the in situ Raman spectra show that the peak corresponding to reconstructed CoFe oxyhydroxide on the surface of SC8F5 is much weaker than that of SC8F2 after 500 cycles (Figure 11i), suggesting low-degree reconstruction for SC8F5 due to the Sr leaching mitigated by segregated Fe_xO_y phase. Similarly, Vojvodic et al. confirmed that the rapid leaching of SrRuO_3 (SRO) under OER conditions can be suppressed by inserting SRO cell beneath a SrTiO_3 (STO) capping layer.^[116] The one-unit cell composed of SRO beneath two layers of STO exhibits superior durability as the Ru sites in the internal structure are not directly combined with the oxygen-containing intermediates. In addition, the introduction of SRO also could motivate STO to exhibit high OER activity due to the upshifted energy level of electrons, suggesting the synergistic effect in the heterostructure. These examples confirm that the reconstruction behavior of pre-catalysts can be regulated by construction of heterostructure.

In conclusion, the electronic properties and distribution of active species in heterostructure could be turned by interface effect, which is beneficial to promoting the reconstruction during the catalytic reaction. Thus, exploring the effect of interface on reconstruction during reaction conditions would be of great research significance.

4.6. Deep Reconstruction

According to the points discussed above, it is evident that an amorphous shell can be formed on the surface of the pre-catalysts during surface reconstruction, which can act as the crucial species for enhanced OER performance. However, the structure transformation only occurs on the surface of the electrocatalyst, resulting in inadequate utilization of internal components, restricted electrochemical active area, and limited mass transfer process.^[6a] Therefore, promoting the reconstruction process and maximizing the generation of active species would be the crucial key to significantly enhancing the utilization rate and specific activity of pre-catalyst components. Furthermore, the reconstruction degree is closely related to material properties, structural modification, and reaction conditions.

The pre-catalysts consisting of etchable species, such as metal-organic frameworks (MOFs),^[117] metal phosphide,^[118] and molybdate,^[119] could easier undergo complete reconstruction under certain reaction conditions. For example, Huang et al. revealed the real active species for superior OER activity in the hybrid Ni-MOF@Fe-MOF .^[120] It was confirmed that the Ni-MOF@Fe-MOF undergoes complete transformation into the complex species composed of NiO , NiOOH , and Fe_2O_3 , which acted as active species for the OER. Lee et al. further discussed the effect of applied potential range on reconstructing zeolitic imidazolate framework-67 (ZIF-67).^[121] As shown in Figure 12a, the applied potential window could impact the Co species' oxidation path and morphological evolution during CV

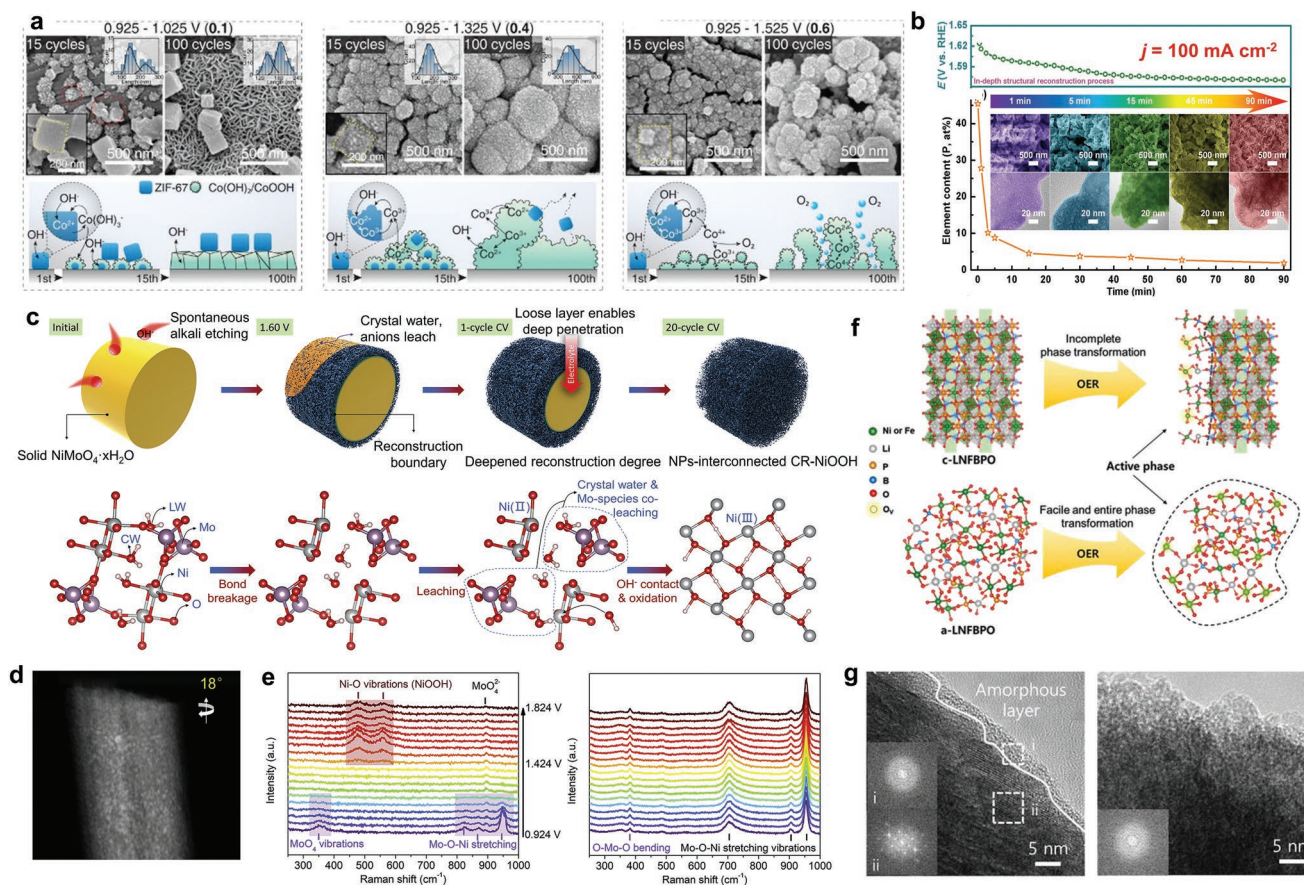


Figure 12. a) The SEM images of ZIF-67 collected at 15 and 100 cycles and corresponding schematic reconstruction process during the different potential range. Reproduced with permission.^[121] Copyright 2020, American Chemical Society. b) Chronopotentiometry curve at 100 mA cm⁻² and P content of Co_{0.8}Fe_{0.2}OOH@C at different electrochemical oxidation time (inset: the corresponding SEM and TEM images). Reproduced with permission.^[43] Copyright 2020, Wiley-VCH. c) Schematic reconstruction process and corresponding crystal evolution of NiMoO₄·H₂O. d) HRTEM image of NiMoO₄·H₂O after complete reconstruction. e) In situ Raman spectra of NiMoO₄·H₂O (left) and NiMoO₄ (right). Reproduced with permission.^[124] Copyright 2020, Elsevier. f) Crystal structures and g) HRTEM images of c-LNFBPO and a-LNFBPO after reconstruction. Reproduced with permission.^[125] Copyright 2021, Wiley-VCH.

activation. As the potential range extended to 0.6 V, the ZIF-67 would be converted thoroughly into CoOOH structure with rich pores caused by the release of oxygen. Fischer et al. found that NiFe surface-mounted metal-organic frameworks (SURMOFs) could undergo specific in situ reconstruction and self-activation process induced by a partial leaching of the deprotonated terephthalic acid linkers,^[122] forming heterostructured NiFe (oxy) hydroxide with optimized OER activity. In particular, introduction of phosphate groups is more conducive to deepening the reconstruction degree. Liu et al. synthesized CoFe(H₃O)(PO₄)₂ nanosheets by in situ electrochemical oxidizing CoP nanosheets in (NH₄)Fe₂(SO₄)₂ electrolyte,^[123] which could be converted to Co_{0.5}Fe_{0.5}OOH through deep self-reconstruction accompanied with oxidation of Co²⁺ and leaching of phosphate anions. The high content of Fe in reconstructed species could form Fe³⁺–O–Fe³⁺ motifs to enhance the OER activity.

The complete reconstruction of metal derivatives can be easily induced assisted by structural regulation. Recently, Qiu et al. found that the Co_{0.8}Fe_{0.2}P@C could be completely converted into highly active Co_{0.8}Fe_{0.2}OOH@C through deep reconstruction accompanied by phosphorous leaching under

OER condition.^[43] Figure 12b exhibits the gradual decline of the applied overpotential for OER along with the entire reconstruction of Co_{0.8}Fe_{0.2}P@C nanosheets into Co_{0.8}Fe_{0.2}OOH@C following the electrochemical oxidation. Moreover, the reduction of phosphorus atomic content to 1.96 at% suggests the almost complete reconstruction. In stark contrast, the reconstruction of crystal CoFe-LDH as a precursor is only limited on the surface. In addition, Selomulya et al. fabricated the core-shell catalyst in which NiFe/NiFeO_x nanoparticles are embedded in N-doped carbon coated on the NiMoO₄ nanorods (NiMoFeO@NC) via pyrolysis of NiMoO₄@PBA,^[126] which could enable its complete reconstruction during the OER process. This conversion strategy can create rich voids and defects in NiMoFeO@NC so that the electrolytes can easily permeate into inner pre-catalysts, resulting in rapid dissolution of MoO₄²⁻ and incorporation of Fe in the active layer to form NiFeOOH/NiFe-LDH species. In addition, the presence of NC can accelerate the electron transfer between active species and oxygen-containing intermediates for OER, which would achieve remarkable enhancement in OER activity. Based on the above demonstrations, it can be summarized that the reconstruction degree can be deepened

by facilitating the dissolution of unstable components in pre-catalysts under reaction conditions.

In addition, the rapid co-leaching of multicomponents in pre-catalysts could loosen the electrocatalyst surface, which is conducive to electrolyte penetration and further etching of inner species. For example, Mai et al. recently found that the introduction of 2-methylimidazole (2-mim) into NiFe polyoxomolybdate ($\text{Fe}_x\text{Ni-POMo}$) would induce the complete construction under OER conditions.^[127] The deep reconstruction degree originates from the low-crystalline and porous features of $\text{Fe}_x\text{Ni-POMo}$, which could facilitate the co-leaching of MoO_4^{2-} and 2-mim ligands and promote the formation of active NiOOH species for OER. The group also reported the complete reconstruction of $\text{NiMoO}_4 \cdot x\text{H}_2\text{O}$ induced by the co-dissolution of MoO_4^{2-} and crystal water. During the electrochemical oxidation process,^[124] the amorphous NiOOH layer is gradually formed on the surface of $\text{NiMoO}_4 \cdot x\text{H}_2\text{O}$, which results in a loose surface structure that further allows the penetration of alkali electrolyte into the inner structure and thereby facilitates the continuous co-leaching of MoO_4^{2-} and crystal water, eventually leading to the complete reconstruction of $\text{NiMoO}_4 \cdot x\text{H}_2\text{O}$ within 20 CV cycles (Figure 12c). The HRTEM images (Figure 12d) reveal that the reconstructed species are composed of ultrafine nanoparticles connected with each other, generating rich interfacial pores. The reconstruction process can be reflected by in situ Raman analysis. As displayed in Figure 12e, the peaks assigned to MoO_4^{2-} vibration and Mo-O-Ni stretching decay dramatically as the applied potential increases during the initial stage of electrochemical oxidation, and then the peaks of NiOOH species appear at large potentials. In contrast, the Raman peaks of NiMoO_4 are always observable in the Raman spectra of NiMoO_4 during the whole reaction process. These results indicate that the co-leaching of MoO_4^{2-} and crystal water plays a critical role in rapid and deep reconstruction of $\text{NiMoO}_4 \cdot x\text{H}_2\text{O}$. The slow reconstruction of NiMoO_4 could be because that the active layer formed on the NiMoO_4 is too dense that hinders further electrolyte penetration. In addition, the complete reconstruction of NiMoO_4 could be achieved under alkaline water electrolysis at industrial operating temperatures of 51.9 °C,^[128] suggesting that the dissolution of MoO_4^{2-} is influenced by temperature.

The complete reconstruction is more likely to occur on the catalysts with large surface area, bringing more species exposed to the solution that allow further transition. Mai et al. adopted the lithiation method to reduce the size of NiO nanoparticles, which would enlarge the surface area and expose more species to the electrolyte, resulting in deep reconstruction into NiOOH nanosheets under electrochemical oxidation.^[129] For comparison, the reconstruction of pure Ni particles with sizes of 100–400 nm only occurs on the surface and forms Ni@NiOOH due to the limited contact area. The rich NiOOH active sites and defects obtained by deep reconstruction performed more excellent mass activity than Ni@NiOOH. Besides, amorphization of catalysts is also an effective method to improve the contact area of the pre-catalyst. Compared with crystalline catalysts, the rich defects and disordered arrangement caused by amorphization facilitate the penetration of the electrolyte into the inner layer of the pre-catalysts and consequently promote the reconstruction degree. For example, Shao et al. converted crystalline $\text{SrCo}_{0.85}\text{Fe}_{0.1}\text{P}_{0.05}\text{O}_{3-\delta}$ (SCFP) into amorphous SCFP under

high-energy argon plasma.^[130] The amorphous SCFP undergoes rapid reconstruction in <2 min due to fast breakage of the weak chemical bonds. Similarly, Song et al. achieved complete reconstruction of LiNiFe boron phosphate (*a*-LNFBPO) during the OER process by the amorphization method,^[125] in sharp contrast to the surface reconstruction of crystalline LiNiFe borophosphate (*c*-LNFBPO) (Figure 12f). It can be found that the amorphization method could cause the shrinkage of metal–oxygen bonds and increase the valence states of metal sites in *a*-LNFBPO, suggesting tuned electronic structure by amorphization could lower the required energy for the formation of active species. The TEM images (Figure 12g) show the existence of a reconstructed amorphous phase at both the surface and inside of *a*-LNFBPO, while the amorphous layer only formed on the surface of *c*-LNFBPO after activation. The amorphous structure enables easy diffusion of OH^- into inside pre-catalysts for deep reconstruction and hosts abundant oxygen vacancies, facilitating the deprotonation of oxygen-containing intermediates on the electrocatalyst surface. Consequently, complete reconstruction exhibits excellent application foreground due to the advantages of maximum utilization and structural optimization of active species. However, complete reconstruction could lead to the decrease in mechanical strength of catalysts and the loss of the synergistic effect. How to avoid these negative effects on catalytic performance remains to be explored.

5. Reconstruction Strategies for HER Electrocatalysts

Similar to OER electrocatalysts, some HER electrocatalysts also undergo reconstruction process to generate new active species or new structures. In this section, we will discuss some of the effective strategies to induce and further to promote the reconstruction reaction of HER electrocatalysts.

5.1. Surface Activation

The electrochemical activation including electrochemical reduction and oxidation is an effective method to induce the reconstruction of HER electrocatalysts. Recently, several reports have found that the metal substance in catalysts would be reduced to lower valence state species under negative potential conditions. Wei et al. found that the Ni-S species on the surface of $\text{Ni}_3\text{S}_2/\text{FeNi}_2\text{S}_4$ would be reduced to metallic Ni₀ species after CV activation.^[131] Similarly, Zhao et al. revealed that the surface reconstruction of NiCoP pre-catalysts into metallic Ni and Co species for HER.^[132] In addition, Sun et al. prepared $\text{Co}_{0.5}\text{W}_{0.5}\text{S}_x$ as pre-catalyst and revealed the pH-dependent bulk and surface structural evolution during the HER.^[133] They found that Co sulfide in the bulk partially transformed to CoO in neutral and alkaline electrolytes, while in acidic electrolyte the Co sulfide can remain initial state. Whereas the surface Co sulfides were reconstructed to $\text{CoO}/\text{Co}(\text{OH})_2$ in the full-pH electrolyte. Meanwhile, the W sulfides in the bulk were transformed to highly distorted WO_x with a lower oxidation state of W in the full-pH electrolyte. WO_x was formed at the surface during the HER in acidic and neutral electrolytes, while only WO_4^{2-} was observed

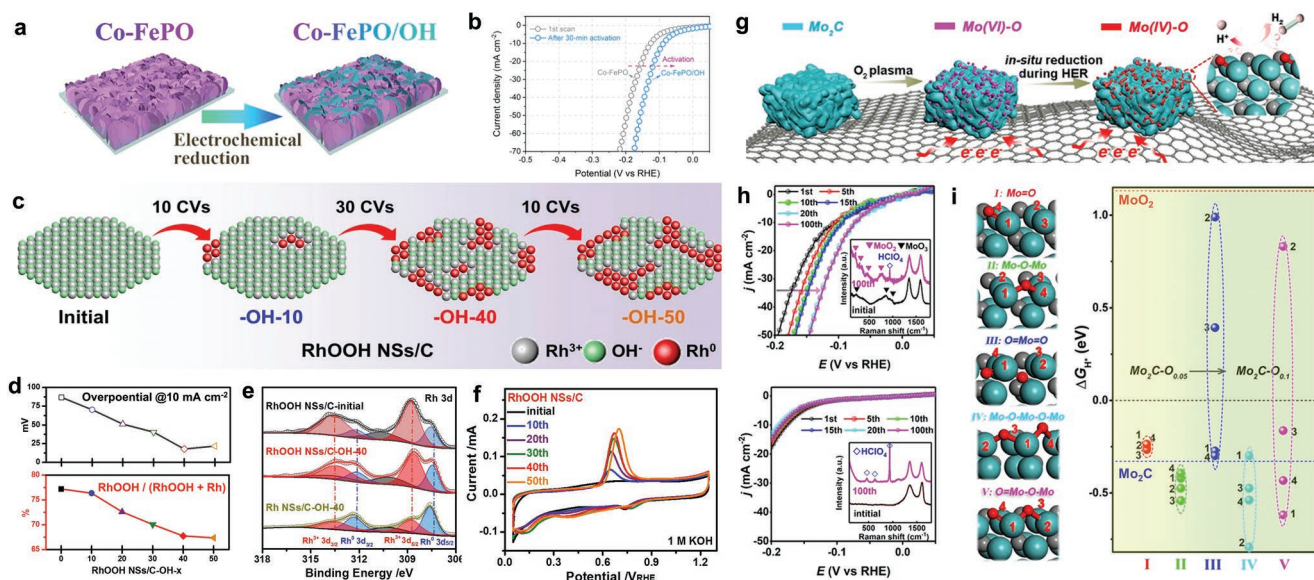


Figure 13. a) Schematic showing the evolution of Co-FePO through electrochemical reduction. b) LSV curves of Co-FePO before and after electrochemical activation. Reproduced with permission.^[134] Copyright 2021, American Chemical Society. c) Structural evolution of RhOOH/C during the electrochemical activation. d) Overpotential at 10 mA cm⁻² and the ratio of Rh/(RhOOH+Rh) as a function of the CV activation cycles. e) Rh 3d XPS spectra of RhOOH/C, RhOOH-OH/C, and Rh-OH/C. f) CO stripping curves of RhOOH/C at different CV activation cycles. Reproduced with permission.^[136] Copyright 2020, Elsevier. g) Synthetic process of Mo₂C-MoO_x/CC. h) LSV curves of Mo₂C-MoO_x/CC (top) and Mo₂C/CC (bottom) (inset: Raman spectra before and after CV activation). i) Models of various Mo oxide sites and corresponding adsorption free energy (ΔG_{H^+}) of H_{ads} on the surface sites. Reproduced with permission.^[137] Copyright 2020, Wiley-VCH.

in the alkaline electrolyte. This work suggests that the structural transformation of pre-catalysts during the HER is highly dependent on the properties of pre-catalysts and electrochemical reaction conditions (e.g., pH).

The discovery of structural evolution during the HER would contribute to the synthesis of high-activity HER reconstructed catalysts. For example, Amal et al. presented the in situ electrochemical reduction of the Co-Fe phosphate (Co-FePO) to Co-Fe (oxy)hydroxide layers on the surface by applying a reduction potential of -0.17 V versus RHE for 30 min in 1 M PBS.^[134] As shown in **Figure 13a,b**, the yielded phosphate/(oxy)hydroxide heterostructure (Co-FePO/OH) electrode exhibited enhanced HER activity in neutral solution. Xia et al. studied the HER activity of reconstructed Co(OH)_x layer formed by surface activation of CoP using the galvanostatic method.^[135] The formed Co(OH)_x layer can promote the water dissociation and strengthen the absorption of H⁺ on active sites of CoP, therefore enhancing the HER performance. Huang et al. reported the RhOOH/Rh interface, formed by the partial electrochemical reduction of RhOOH nanosheets (NSs), plays a vital role in the obtained superior HER performance.^[136] As shown in **Figure 13c**, the RhOOH was gradually reduced into metallic Rh with increased activation cycles up to 40 cycles, resulting in the enhancement of HER activity (**Figure 13d**). The transition of RhOOH into Rh can be confirmed by the increase in CO stripping peaks (**Figure 13e**) and Rh⁰ XPS peaks (**Figure 13f**). It can be noted that the best HER performance was achieved at 40 CV cycles due to the presence of a reasonable Rh/RhOOH interface, which can significantly decrease the water dissociation energy and adsorption energy of the H atoms on Rh sites.

The surface reconstruction of HER catalysts to achieve higher catalytic activity can be also achieved by electrochemical oxidation of the pre-catalysts. Mi et al. proposed an in situ electrochemical transformation strategy to design Ni₂P-CoOOH electrocatalytic system, where the CoOOH 2D nanosheets were decorated on Ni₂P nanotube arrays.^[138] The formation of CoOOH nanosheets on Ni₂P can modify the distribution of local density of states induced by the electron transfer from Ni₂P to CoOOH. As a result, the free Gibbs energy of H⁺ adsorption on Ni₂P-CoOOH is close to the thermodynamic neutral value, which ensures a high HER activity. These results are consistent with the conclusion that the interfacial charge transfer behavior can regulate the local electronic structure of the active sites and promote the dissociation of water molecules along with the desorption of hydrogen atoms. Electrochemical activation could modify the surface chemical properties of pre-catalysts for enhanced HER activity, but the effect of electrochemical operation conditions (e.g., cycling number, applied potential range, or current density) on the reconstruction process and HER activity of the reconstructed species is not thoroughly studied yet.

Plasma-assisted activation has opened another efficient avenue for promoting the HER catalytic activity of electrocatalysts. Under the physical plasma bombardment, light elements could be extracted from the materials. Cheng et al. reported that the Ar plasma treatment of MoSe₂ can create holes and vacancies and thus enhance the HER efficiency.^[139] Similar to the electrochemical activation, the plasma activation can also modify the surface properties by introducing functional groups or generating new species but without changing the bulk properties of the catalysts. Chueh et al. applied gaseous

selenium plasma to convert the Mo surface into MoSe₂, resulting in a MoSe₂/Mo core-shell nanostructure. The heterostructure possessed a low onset potential of −89 mV versus RHE, which can be explained by the high density of exposed active sites and metallic conductivity of MoSe₂ shell.^[140] He et al. designed Mo₂C-MoO_x heterostructure grown on carbon cloth (Mo₂C-MoO_x/CC) by partial oxidation of Mo₂C through oxygen plasma treatment as highly effective electrocatalysts for HER (Figure 13g).^[137] As displayed in Figure 13h, the HER LSV curves of Mo₂C-MoO_x/CC gradually shift to the lower potentials as the activation cycles increase. However, the trend is not apparent for Mo₂C/CC, indicating the positive effect of MoO_x on the electrochemical reconstruction of Mo₂C/CC. Moreover, the surface Mo(VI) species in initial Mo₂C-MoO_x were reduced to Mo(IV) species during the HER, which can be manifested by the in situ Raman spectroscopy that the peaks of the bands associated with MoO₃ in Mo₂C-MoO_x disappeared, while the peaks assigned to MoO₂ could be observed after CV activation. In sharp contrast, there was a negligible surface evolution in Mo₂C during the HER process. Based on the DFT calculations (Figure 13i), introducing oxygen atoms to Mo₂C could effectively reduce the free energy for generation of H⁺. The effect of plasma treatment time on the HER activity was also studied, and the result shows that the optimal HER activity of catalysts is achieved at 2 min, while further oxidation of Mo₂C is unfavorable to catalytic activity, which is in agreement with the DFT results. This work suggests the great potential of plasma activation to promote surface reconstruction during catalysis.

5.2. Partial Dissolution

Partial dissolution of less stable components in pre-catalysts is an effective approach to realize reconstruction of highly active species, not only for the OER but also for the HER catalyst. For example, Lu et al. synthesized ZnCo phosphate as HER electrocatalysts and revealed that the reconstruction of Co²⁺-rich hydroxide was induced by electrochemical etching of PO₄³⁻ and

Zn²⁺.^[141] The resulting interface between the ZnCo phosphate and cobalt hydroxyl oxide was proved to promote the charge transfer from atomic Co to the surrounding environment, thus increasing the HER activity. Shao et al. developed conductive monoclinic SrIrO₃ perovskite as excellent HER electrocatalysts and revealed the pivotal role of lattice Sr²⁺ leaching in triggering the self-reconstruction.^[142] As displayed in Figure 14a,b, the species on the surface of SrIrO₃ perovskite were transformed into metallic Ir species during activation process accompanied by leaching of lattice Sr²⁺, which is likely responsible for the enhanced activity of the reconstructed SrIrO₃ electrocatalysts. In sharp contrast, the IrO₂ catalyst exhibited a highly stable surface structure in the HER process. Similarly, Cho et al. fabricated a novel Ir-based perovskite electrocatalyst composed of quasi 2D Sr₂IrO₄ and 3D 6H phase SrIrO₃ perovskites,^[143] in which the interlaminar Sr²⁺ easily extracted from the crystal Sr₂IrO₄ while maintaining the in-plane IrO₆ octahedral framework, thus stabilizing the Ir state and exposing rich active sites for HER.

Interestingly, some dissolved species induced by partial dissolution could re-deposit onto and react with the catalysts to form highly active species under the HER conditions. Ho et al. fabricated Co particles wrapped with N-doped carbon nanotubes on the CoMoO₄ nanosheets arrays to obtain Co@NCNT/CoMoO₄ pre-catalysts and induce the fast dissolution of MoO₄²⁻ to yield reconstructed Co@NCNT/CoMoO₄ under in situ electrochemical oxidation.^[144] As illustrated in Figure 14c, it could be identified that partially dissolved MoO₄²⁻ ions were deposited back to the parent electrode at negative voltage and then polymerize to form Mo₂O₇²⁻, which were further converted into Mo-Mo species on the surface. The resulting Mo-Mo species enabled the excellent HER kinetics in alkaline solution and seawater. The “dissolution–re-deposition” path was also demonstrated in reconstructing Cu-Fe₃O₄ catalyst prepared by Yang et al. (Figure 14d).^[145] During the electrochemical activation process, part of the Fe₃O₄ species was leached at the catalyst-electrolyte interface and reacted with OH⁻ to form an amorphous FeOOH phase on the precursor surface. By introducing

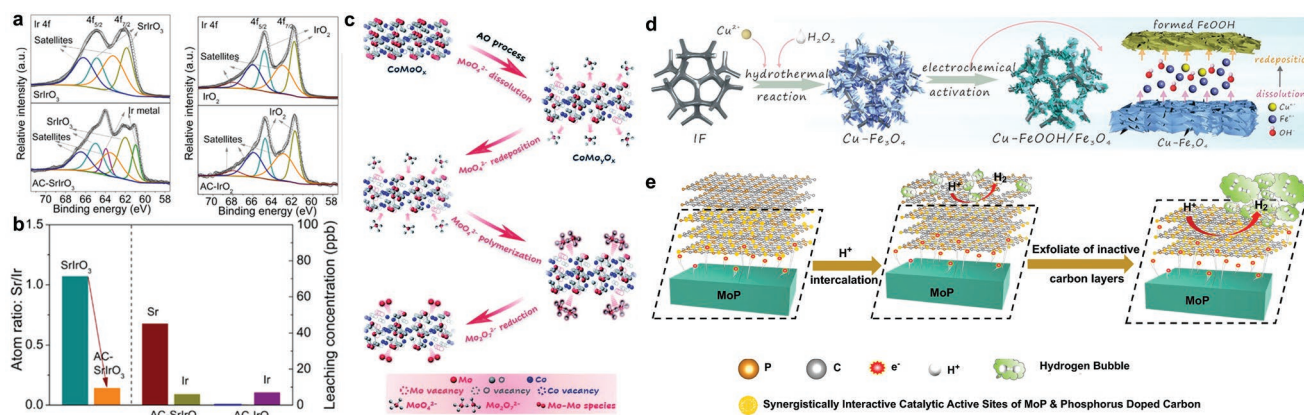


Figure 14. a) Ir 4f XPS spectra of SrIrO₃ and IrO₂ before and after electrochemical activation. b) Surface atom ratio of Sr/Ir in SrIrO₃ and AC-SrIrO₃ (left) and leaching concentration of Sr and Ir in SrIrO₃ and IrO₂ after electrochemical activation (right). Reproduced with permission.^[142] Copyright 2020, American Chemical Society. c) Evolution of Co@NCNT/CoMoO₄ under in situ electrochemical oxidation. Reproduced with permission.^[144] Copyright 2022, Royal Society of Chemistry. d) Synthesis of Cu-Fe₃O₄ catalysts and their transformation to Cu-FeOOH/Fe₃O₄ during electrochemical activation. Reproduced with permission.^[145] Copyright 2022, Wiley-VCH. e) Evolution of phosphorus-doped carbon@MoP electrocatalysts during reconstruction process. Reproduced with permission.^[146] Copyright 2021, Springer.

the defective FeOOH on the surface of the Cu-Fe₃O₄ catalyst through electrochemical activation, the energy barriers for H₂O decomposition and H₂ generation were reduced. This surface self-reconstruction strategy provides a new approach for the production of efficient non-noble metal HER catalysts. Moreover, carbon layers can also be etched to form highly reactive electrochemical surfaces. Wang et al. proposed an electrochemical-induced surface reconstruction strategy to prepared phosphorus-doped carbon@MoP electrocatalysts with excellent activity for HER.^[146] As shown in Figure 14e, the inactive surface carbon layer was exfoliated in harsh acidic solution during the CV process as a result of proton intercalation. Meanwhile, electrons flow from the MoP to the inner carbon layer, which significantly reduces the adsorption free energy of H*. In addition, the synergistic interface between MoP and P-doped carbon greatly accelerated the proton/electron transfer and hydrogen dissociation, which was ultimately beneficial to the whole reaction process. This work provides a promising in situ electrochemical etching strategy for constructing highly active catalytic species.

Partial dissolution of pre-catalysts not only leads to surface reconstruction but sometimes also deep reconstruction. Mu et al. fabricated surface F-enriched CoF₂ with a hydrophilic characteristic,^[147] which exhibited continuous self-reconstruction property. Due to the high ionic properties, F⁻ ions would be rapidly leached out of the lattice of CoF₂ once in contact with the alkaline electrolyte, while OH⁻ immediately coordinated with Co atoms to form amorphous α -Co(OH)₂, which was then rapidly transformed to amorphous β -Co(OH)₂. The reconstruction would continuously proceed until all the F⁻ ions were leached out. The as-obtained β -Co(OH)₂ possesses abundant active sites and short charge transfer paths, leading to excellent

HER activity. Deep reconstruction often leads to significantly distorted structures and thus abundant active sites, which is worth further exploration. Unfortunately, currently there has been only a few successful examples. In this regard, effective and general strategies to initiate the deep reconstruction should be developed.

5.3. Ionic Doping

Ionic doping can promote the reconstruction of pre-catalysts to form HER reactive species. For example, Chai et al. found that the W incorporation could promote the in situ cathodic activation of FeP_x.^[148] The enhanced reconstruction performance was attributed to the regulating effect of W dopants on the coordination environment of the pre-catalysts. Zhang et al. reported that certain Fe substitution can enhance the structural flexibility and accommodate more sulfur vacancies in NiS₂ to lower the applied potential threshold for phase reconfiguration of NiS₂ to Ni₂S₃, and further reduce the onset overpotential for HER (Figure 15a).^[149] As shown in Figure 15b, the substituted Fe in NiS₂ raised the S 3p band center energy to be closer to the Fermi level, reducing the energy barrier for the formation of S vacancy. Meanwhile, with the Fe substitution, the overlap of Ni 3d and S 3p band is increased and the Fermi level decreases, which created ligand holes to release S from the system, resulting in S vacancies. Besides cations, doping pre-catalysts with anions could also produce abundant vacancies/defects and promote the reconstruction process. Chen et al. confirmed the promoting effect of P substitution on the reconstruction of cubic CoSe₂ (*c*-CoSe₂) for HER.^[150] As displayed in Figure 15c, the structural component in the *c*-CoSe₂ retains the initial

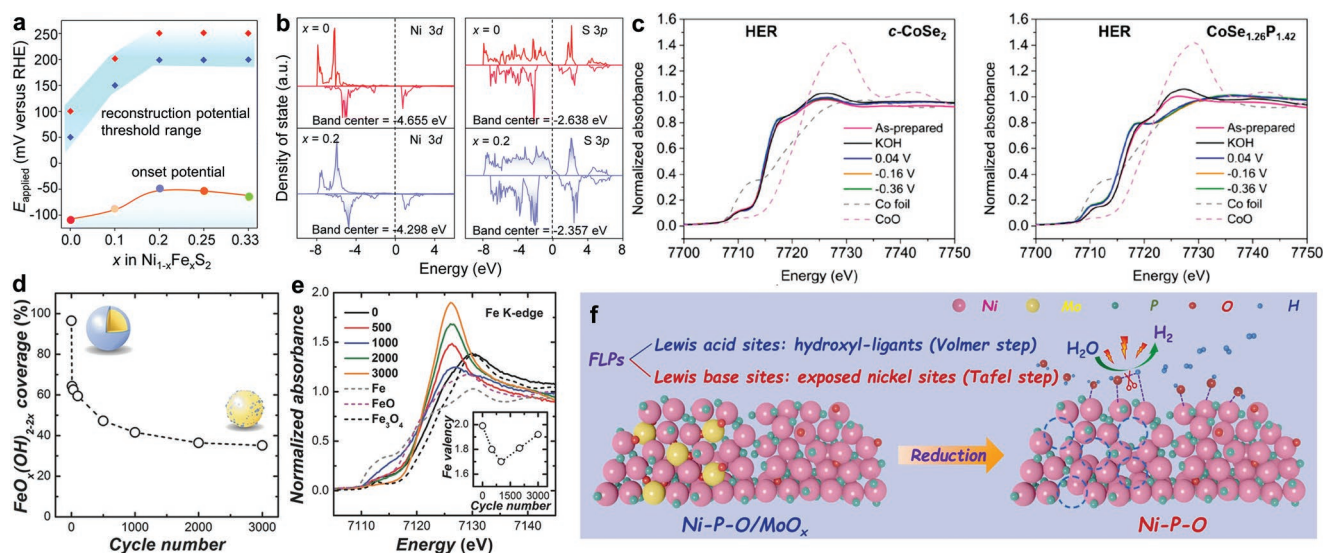


Figure 15. a) The surface reconstruction potential threshold range of the Ni_{1-x}Fe_xS₂ samples and the corresponding onset potentials of HER. b) Ni 3d and S 3p projected density of state of Ni_{1-x}Fe_xS₂ ($x = 0.0, 0.2$). Reproduced with permission.^[149] Copyright 2022, Royal Society of Chemistry. c) In situ XANES of *c*-CoSe₂ and CoSe_{1.26}P_{1.42} during HER process. Reproduced with permission.^[150] Copyright 2019, American Chemical Society. d) FeO_x(OH)_{2-2x} coverage of Pd/FeO_x(OH)_{2-2x} at different activation cycles. e) Fe K-edge XANES spectra of Fe, FeO, Fe₃O₄, and FeO_x(OH)_{2-2x} activated at different cycles (inset: the Fe valency state obtained at different cycles). Reproduced with permission.^[151] Copyright 2017, Wiley-VCH. f) Evolution of Ni-P-O/MoO_x to generate Ni-P-O during HER process and enhanced mechanism of catalytic activity Ni-P-O for alkaline HER. Reproduced with permission.^[152] Copyright 2022, Elsevier.

state during the HER process owing to the inhibition of the reconstruction by the stable cubic structure and the presence of selenium. In stark contrast, the $\text{CoSe}_{1.26}\text{P}_{1.42}$ was reduced to metallic Co species after HER process, which can be attributed to the abundant vacancies/defects introduced by P substitution, enabling Co cations in $\text{CoSe}_{1.26}\text{P}_{1.42}$ to be easily reduced.

In addition, the dopants in reconstructed species can also affect the HER activity. Patzke et al. developed Fe-doped cobalt phosphide nanoboxes as pre-catalysts and revealed that the partial Fe substitution promotes a structural reconstruction into P-Co-O-Fe-P species with low-valence metal centers during the HER process,^[153] which can reduce the energy barrier for water dissociation and facilitate the adsorption/desorption of HER intermediates, resulting in excellent HER performance. Zhou et al. fabricated V-doped CoO nanosheets via cathode electrochemical activation of amorphous VCo bimetallic oxide precursor.^[154] During the reconstruction process, the V^{5+} would dissolve in electrolyte, while V^{4+} would be doped into CoO and effectively enhance the intrinsic activity of oxides.

As a kind of compositional modulation method, ionic doping can promote reconstruction process and the formation of highly active species for HER. Nevertheless, the relationship between dopants and reconstruction kinetics remains to be further explored.

5.4. Heterostructure Construction

Reconstruction process could be promoted by interface effect in heterostructures. For example, cobalt carbonate hydroxide (CoCH) with TiO_2 coating after in situ surface reconstruction via repeated LSV scans [$\text{TiO}_2@\text{CoCH}$ (A)] in alkaline HER conditions showed much higher HER activity than CoCH after the same electrochemical activation [CoCH (E)] and TiO_2 .^[155] The coupling with TiO_2 could promote the formation of interstitial Co defects accompanied with the reduction of Ti during the HER process, resulting in a low Gibbs free energy for the Volmer step in the HER process and thus enhancing the HER activity. Similarly, the TiO_2 coating on $\text{Co}_2\text{P}_4\text{O}_{12}$ can weaken the P-O bonds in PO_4^{3-} ,^[156] promoting the transformation from $\text{Co}_2\text{P}_4\text{O}_{12}$ into $\text{CoO}_x(\text{OH})_y$, which would be reduced to metallic Co species that show HER activity during the catalytic process. The introduction of TiO_2 with abundant oxygen vacancies can also facilitate the water dissociation on active sites during the HER process.

In some heterostructure systems, the inactive compositions may transform into functional species, supporting active species for higher catalytic activity. For instance, Liao et al. designed $\text{Pd}/\text{FeO}_x(\text{OH})_{2-2x}$ core/shell composite through reconstruction of $\text{Pd}/\text{Fe}_3\text{O}_4$. It was found that the $\text{FeO}_x(\text{OH})_{2-2x}$ shell can serve as the proton supply to promote the HER activity in alkaline solution.^[151] The $\text{FeO}_x(\text{OH})_{2-2x}$ coverage and Fe valance state can be modified by controlling the electrochemical cycling numbers, as shown in Figure 15d,e. The appropriate $\text{FeO}_x(\text{OH})_{2-2x}$ coverage can facilitate water dissociation and produce more H intermediates, which would be transferred to the Pd nanoparticle's surface and converted to H_2 gas, resulting in excellent HER kinetics. Xie et al. found that H_xWO_3 converted by H^+ insertion of WO_3 during the reconstruction process

under negative potentials can serve as electron conductor and H^+ transfer channels to Pt catalytic sites in $\text{Pt}/\text{H}_x\text{WO}_3$ heterostructures.^[157] The Pt promotes the H^+ insertion in WO_3 to form H_xWO_3 , facilitating the hydrogen adsorption/desorption on Pt sites. The $\text{Pt}-\text{WO}_3$ possesses excellent electronic conductivity with fast reaction charge transfer on the interface between electrolyte and catalyst, resulting in a high coverage of H intermediates on the catalysts surface and thus improved HER kinetics.

In addition, the synergistic effect of heterogeneous components can also enhance the activity of the reconstructed species. Yang et al. synthesized broccoli-like hierarchical $\text{Ni}_2\text{P}-\text{Ni}(\text{PO}_3)_2$ nanoparticles on vertical monocrystalline NiMoO_4 nanorods,^[152] which effectively integrate artificial frustrated Lewis pairs (FLPs) after reconstruction process. As shown in Figure 15f, dissolution of MoO_x further exposed more Ni sites as Lewis base sites to promote the adsorption of H^* during the Tafel step, while hydroxyl ligands in situ formed on the surface of the loaded nanoparticles as Lewis acid sites to boost the activation of H_2O molecules. The FLPs achieved low overpotentials of 11 and 79 mV at 10 and 100 mA cm^{-2} . Although construction of heterostructure was widely applied as an effective modified strategy to design high-performance electrocatalysts,^[158] its use in promoting the catalysts' reconstruction is still limited and the effects of multiple components of the heterostructure on reconstruction process and further the HER activity are still not fully understood.

6. Conclusion and Outlook

With the development of ex situ and in situ characterization techniques in recent years, the dynamic reconstruction processes can be studied in detail. This paper gives a comprehensive review on recent research advances in the basic principle of water electrolysis, the characterizations of reconstruction phenomenon, and the regulation strategies of reconstructed electrocatalysts. Through modification strategies such as defect engineering, partial dissolution, ion doping, and heterostructure construction, the structural flexibility and electronic properties of the pre-catalysts can be tuned to exhibit greatly improved conductivity, promoted electron transfer rate, and reduced energy barrier required for the formation of active species. By optimizing the phase and electronic structure of the pre-catalysts supplemented by activation methods including electrochemical and plasma activation, the transition rate and degree of reconstruction as well as the catalytic activity of the formed active species can be greatly enhanced, resulting in highly efficient water splitting electrocatalysts. However, the development of efficient reconstructed electrocatalysts suitable for large-scale application remains a huge challenge. The activity and stability of reconstructed electrocatalysts for OER or HER should be further improved. Several remaining challenges are listed as follows:

- 1) Understanding the mechanism of reconstruction is necessary for the design of highly active reconstructed catalysts. In particular, the regulation mechanism on the electronic structure and catalytic activity of the corresponding reconstructed species requires further exploration. DFT calculation should

be applied more to reveal the reaction energetics in the reconstruction process. In addition, the complex composition of the reconstructed catalysts introduces additional difficulty in the exploration of catalytic mechanisms and the recognition of real catalytic sites. Hence, more accurate characterizations (such as femtosecond time-resolved transient absorption spectroscopy, in situ electron microscopy, and scalable X-ray absorption fine-structure techniques) are required to understand the function of each component in the reconstruction process and in turn guide the design of active components with the optimized synergistic effect.

- 2) For pre-catalysts with weak stability, such as perovskites and MOFs, the reconstruction process could potentially destroy the internal structure due to the severe dissolution of components, resulting in the loss of active sites. Therefore, inhibiting the dissolution of these active species, but at the same time, without significantly affecting the reconstruction process, is the key to maintaining the pre-catalysts' high catalytic activity and stability. This might be solved by introducing additional elements or chemical groups to stabilize the bulk structure, or by coating the catalysts with protective layers.
- 3) Considering that the reconstructed species that serve as the real active sites for OER or HER, the catalytic performance would be gradually enhanced as more reconstructed species formed. However, the reconstruction usually occurs only at the near-surface region of the catalysts that results in reconstructed layers of <10 nm thick. Therefore, enhancing the reconstruction degree of pre-catalysts to promote the generation of more active sites is worth further exploration. On the other hand, a thickened surface layer might reduce the electronic conductivity and weaken the synergy of the surface active sites and the original "pre-catalysts". Therefore, precisely tuning the reconstruction degree to ensure the maximum utilization of the surface active sites while without sacrificing the intrinsic properties of the "pre-catalysts" (e.g., robust stability, high electric conductivity) is an important direction for future research.
- 4) In most reports, the tests of water electrolysis are usually carried out under room temperature, with low electrolyte concentration and short operation time. However, the operation of industrial water electrolysis systems requires much larger current densities ($0.5\text{--}1.6\text{ A cm}^{-2}$), higher temperature ($40\text{--}90\text{ }^{\circ}\text{C}$), higher electrolyte concentration ($4.2\text{--}6.9\text{ M}$), and longer operation time (over 1000 h). In the two cases, the reconstruction results may be very different, including the reconstruction kinetics, reconstructed active species, and microstructures. In addition, harsh reaction conditions in industrial water electrolyzer require the reconstructed catalysts to achieve higher intrinsic activity and stability. Therefore, it is necessary to evaluate the various performance of catalysts under industrial parameters, especially the changes of intrinsic reactive species, catalytic activity, and catalytic selectivity during the reconstruction process. However, these research issues are rarely reported and deserve more attention, which would benefit the rational design and practical application for reconstructed catalysts.
- 5) Despite recent discussion on the reconstruction mechanisms during the OER process, relatively few reports are

exploring the reconstruction mechanisms under HER conditions. In addition, the reconstruction phenomenon could also be observed in other electrocatalytic processes, such as CO_2 reduction,^[159] oxygen reduction reaction,^[160] and nitrogen reduction.^[161] Exploring the reconstruction mechanisms of other electrocatalytic processes is favorable for expanding the application range of reconstructed catalysts. Finally, since most of the catalytic reconstruction is essentially an electrochemical process, its large-scale preparation could also be a challenge.

Acknowledgements

This work was supported by the Fundamental Research Funds for the Central Universities, China (Grant 20720210010) and Xiamen University.

Conflict of Interest

The authors declare no conflict of interest.

Keywords

electrocatalysts, hydrogen evolution reaction, oxygen evolution reaction, surface reconstruction, water electrolysis

Received: May 19, 2022

Revised: June 24, 2022

Published online: July 8, 2022

- [1] a) R. Q. Yao, Y. T. Zhou, H. Shi, W. B. Wan, Q. H. Zhang, L. Gu, Y. F. Zhu, Z. Wen, X. Y. Lang, Q. Jiang, *Adv. Funct. Mater.* **2021**, 31, 2009613; b) F. X. Jiao, J. L. Wang, Y. Lin, J. H. Li, X. F. Jing, Y. Q. Gong, *Appl. Surf. Sci.* **2021**, 553, 149440.
- [2] X. Li, L. L. Zhao, J. Y. Yu, X. Y. Liu, X. L. Zhang, H. Liu, W. J. Zhou, *Nano-Micro Lett.* **2020**, 12, 131.
- [3] B. M. Hunter, H. B. Gray, A. M. Müller, *Chem. Rev.* **2016**, 116, 14120.
- [4] a) Y. P. Lin, H. Wang, C. K. Peng, L. M. Bu, C. L. Chiang, K. Tian, Y. Zhao, J. Q. Zhao, Y. G. Lin, J. M. Lee, L. J. Gao, *Small* **2020**, 16, 2002426; b) X. Y. Zhang, J. Li, Y. Yang, S. Zhang, H. S. Zhu, X. Q. Zhu, H. H. Xing, Y. L. Zhang, B. L. Huang, S. J. Guo, E. K. Wang, *Adv. Mater.* **2018**, 30, 1803551.
- [5] a) X. K. Huang, X. P. Xu, C. Li, D. F. Wu, D. J. Cheng, D. P. Cao, *Adv. Energy Mater.* **2019**, 9, 1803970; b) J. Wang, Y. Gao, H. Kong, J. Kim, S. Choi, F. Ciucci, Y. Hao, S. Yang, Z. Shao, J. Lim, *Chem. Soc. Rev.* **2020**, 49, 9154.
- [6] a) X. Liu, J. Meng, J. Zhu, M. Huang, B. Wen, R. Guo, L. Mai, *Adv. Mater.* **2021**, 33, 2007344; b) P. F. Liu, H. Yin, H. Q. Fu, M. Y. Zu, H. G. Yang, H. Zhao, *J. Mater. Chem. A* **2020**, 8, 10096.
- [7] L. C. Seitz, C. F. Dickens, K. Nishio, Y. Hikita, J. Montoya, A. Doyle, C. Kirk, A. Vojvodic, H. Y. Hwang, J. K. Nørskov, T. F. Jaramillo, *Science* **2016**, 353, 1011.
- [8] a) Y. Duan, S. Sun, Y. Sun, S. Xi, X. Chi, Q. Zhang, X. Ren, J. Wang, S. J. H. Ong, Y. Du, L. Gu, A. Grimaud, Z. J. Xu, *Adv. Mater.* **2019**, 31, 1807898; b) N. Hong Nhan, T. Reier, H.-S. Oh, M. Gliech, P. Paciok, V. T. Ha Thi, D. Teschner, M. Heggen, V. Petkov, R. Schloegl, T. Jones, P. Strasser, *Nat. Catal.* **2018**, 1, 841; c) W. Zhu, W. Chen, H. Yu, Y. Zeng, F. Ming, H. Liang, Z. Wang, *Appl. Catal. B* **2020**, 278, 119326.

- [9] Y. Lyu, J. Zheng, Z. Xiao, S. Zhao, S. P. Jiang, S. Wang, *Small* **2020**, 16, 1906867.
- [10] a) N. C. S. Selvam, L. J. Du, B. Y. Xia, P. J. Yoo, B. You, *Adv. Funct. Mater.* **2021**, 31, 2008190; b) Y. Y. Li, X. C. Du, J. W. Huang, C. Y. Wu, Y. H. Sun, G. F. Zou, C. T. Yang, J. Xiong, *Small* **2019**, 15, 1901980; c) P. G. Felipe, B. Zhenghong, Z. Xuanyu, H. Weixin, W. Zili, *ACS Catal.* **2019**, 9, 5692.
- [11] M. Yu, E. Budiyo, H. Tüysüz, *Angew. Chem., Int. Ed.* **2021**, 60, 2.
- [12] H. Shi, H. Liang, F. Ming, Z. Wang, *Angew. Chem., Int. Ed.* **2017**, 56, 573.
- [13] a) Y. F. Cheng, L. Niu, *Electrochem. Commun.* **2007**, 9, 558; b) Y. Xu, C. Wang, Y. Huang, J. Fu, *Nano Energy* **2021**, 80, 105545.
- [14] X. Zou, Y. Zhang, *Chem. Soc. Rev.* **2015**, 44, 5148.
- [15] P. Xiao, W. Chen, X. Wang, *Adv. Energy Mater.* **2015**, 5, 1500985.
- [16] X. Huang, X. Xu, X. Luan, D. Cheng, *Nano Energy* **2020**, 68, 104332.
- [17] a) W. Yang, S. Chen, *Chem. Eng. J.* **2020**, 393, 124726; b) R. Zahra, E. Pervaiz, M. Yang, O. Rabi, Z. Saleem, M. Ali, S. Farrukh, *Int. J. Hydrogen Energy* **2020**, 45, 24518.
- [18] L. Zhang, Y. Jia, H. Liu, L. Zhuang, X. Yan, C. Lang, X. Wang, D. Yang, K. Huang, S. Feng, X. Yao, *Angew. Chem., Int. Ed.* **2019**, 58, 9404.
- [19] J. Xie, X. Yang, Y. Xie, *Nanoscale* **2020**, 12, 4283.
- [20] W. Liu, P. Geng, S. Li, W. Liu, D. Fan, H. Lu, Z. Lu, Y. Liu, *J. Energy Chem.* **2021**, 55, 17.
- [21] H. Wang, W. Fu, X. Yang, Z. Huang, J. Li, H. Zhang, Y. Wang, *J. Mater. Chem. A* **2020**, 8, 6926.
- [22] a) N. Zhang, Y. Chai, *Energy Environ. Sci.* **2021**, 14, 4647; b) M. Tahir, L. Pan, F. Idrees, X. Zhang, L. Wang, J. J. Zou, Z. L. Wang, *Nano Energy* **2017**, 37, 136.
- [23] L. Li, P. Wang, Q. Shao, X. Huang, *Adv. Mater.* **2021**, 33, 2004243.
- [24] H. Liang, F. Meng, M. Cabán-Acevedo, L. Li, A. Forticaux, L. Xiu, Z. Wang, S. Jin, *Nano Lett.* **2015**, 15, 1421.
- [25] H. Liang, A. N. Gandi, D. H. Anjum, X. Wang, U. Schwingenschlögl, H. N. Alshareef, *Nano Lett.* **2016**, 16, 7718.
- [26] X. Xu, H. Liang, F. Ming, Z. Qi, Y. Xie, Z. Wang, *ACS Catal.* **2017**, 7, 6394.
- [27] Y. Li, M. Wang, Y. Yi, C. Lu, S. Dou, J. Sun, *Small* **2021**, 17, 2005573.
- [28] a) Q. Y. Ma, C. Y. Hu, K. L. Liu, S. F. Hung, D. H. Ou, H. M. Chen, G. Fu, N. F. Zheng, *Nano Energy* **2017**, 41, 148; b) A. Bergmann, T. E. Jones, E. M. Moreno, D. Teschner, P. Chernev, M. Gliech, T. Reier, H. Dau, P. Strasser, *Nat. Catal.* **2018**, 1, 711; c) J. Huang, Y. Li, Y. Zhang, G. Rao, C. Wu, Y. Hu, X. Wang, R. Lu, Y. Li, J. Xiong, *Angew. Chem., Int. Ed.* **2019**, 58, 17458.
- [29] J. Jiang, Y.-J. Zhang, X.-J. Zhu, S. Lu, L.-L. Long, J.-J. Chen, *Nano Energy* **2021**, 81, 105619.
- [30] a) K. Fan, H. Y. Zou, N. Dharanipragada, L. Z. Fan, A. K. Inge, L. L. Duan, B. B. Zhang, L. C. Sun, *J. Mater. Chem. A* **2021**, 9, 11359; b) J. C. Kim, C. W. Lee, D. W. Kim, *J. Mater. Chem. A* **2020**, 8, 5655; c) W. Du, Y. M. Shi, W. Zhou, Y. F. Yu, B. Zhang, *Angew. Chem., Int. Ed.* **2021**, 60, 7051.
- [31] F. Polo-Garzon, Z. Bao, X. Zhang, W. Huang, Z. Wu, *ACS Catal.* **2019**, 9, 5692.
- [32] a) X. Li, H. Y. Wang, H. Yang, W. Cai, S. Liu, B. Liu, *Small Methods* **2018**, 2, 1700395; b) M. Povia, D. F. Abbott, J. Herranz, A. Heinritz, D. Lebedev, B.-J. Kim, E. Fabbri, A. Patru, J. Kohlbrecher, R. Schaublin, M. Nachtegaal, C. Copéret, T. J. Schmidt, *Energy Environ. Sci.* **2019**, 12, 3038.
- [33] M. Miao, R. Z. Hou, R. J. Qi, Y. Yan, L. Q. Gong, K. Qi, H. F. Liu, B. Y. Xia, *J. Mater. Chem. A* **2019**, 7, 18925.
- [34] M. Mathankumar, S. Anantharaj, A. K. Nandakumar, S. Kundu, B. Subramanian, *J. Mater. Chem. A* **2017**, 5, 23053.
- [35] Z. H. Xiao, Y. C. Huang, C. L. Dong, C. Xie, Z. J. Liu, S. Q. Du, W. Chen, D. F. Yan, L. Tao, Z. W. Shu, G. H. Zhang, H. G. Duan, Y. Y. Wang, Y. Q. Zou, R. Chen, S. Y. Wang, *J. Am. Chem. Soc.* **2020**, 142, 12087.
- [36] G. W. Zhang, J. R. Zeng, J. Yin, C. Y. Zuo, P. Wen, H. T. Chen, Y. J. Qiu, *Appl. Catal. B* **2021**, 286, 119902.
- [37] A. Grimaud, A. Demortiere, M. Saubaniere, W. Dachraoui, M. Duchamp, M. L. Doublet, J. M. Tarascon, *Nat. Energy* **2017**, 2, 16189.
- [38] N. Ortiz Peña, D. Ihiwakrim, M. Han, B. Lassalle-Kaiser, S. Carenco, C. Sanchez, C. Laberty-Robert, D. Portehault, O. Ersen, *ACS Nano* **2019**, 13, 11372.
- [39] T. Susi, C. Hofer, G. Argentero, G. T. Leuthner, T. J. Pennycook, C. Mangler, J. C. Meyer, J. Kotakoski, *Nat. Commun.* **2016**, 7, 13040.
- [40] M. Xia, T. Liu, N. Peng, R. Zheng, X. Cheng, H. Zhu, H. Yu, M. Shui, J. Shu, *Small Methods* **2019**, 3, 1900119.
- [41] Z. H. Yan, H. M. Sun, X. Chen, H. H. Liu, Y. R. Zhao, H. X. Li, W. Xie, F. Y. Cheng, J. Chen, *Nat. Commun.* **2018**, 9, 2373.
- [42] K. Kooser, T. Käämbre, M. Vestli, U. Joost, S. Urpelainen, M. Kook, F. Bournel, J. J. Gallet, E. Lust, E. Kuk, G. Nurk, *Int. J. Hydrogen Energy* **2020**, 45, 25286.
- [43] X. T. Han, C. Yu, Y. Y. Niu, Z. Wang, Y. B. Kang, Y. W. Ren, H. Wang, H. S. Park, J. S. Qiu, *Small Methods* **2020**, 4, 2000546.
- [44] a) C. V. Cushman, P. Brünner, J. Zakel, G. H. Major, B. M. Lunt, N. J. Smith, T. Grehl, M. R. Linford, *Anal. Methods* **2016**, 8, 3419; b) H. H. Brongersma, M. Draxler, M. De Ridder, P. Bauer, *Surf. Sci. Rep.* **2007**, 62, 63.
- [45] L. Zhang, H. Yuan, L. Wang, H. Zhang, Y. Zang, Y. Tian, Y. Wen, F. Ni, H. Song, H. Wang, *Sci. China Mater.* **2020**, 63, 2509.
- [46] R. Nakamura, A. Imanishi, K. Murakoshi, Y. Nakato, *J. Am. Chem. Soc.* **2003**, 125, 7443.
- [47] B. L. Wang, K. N. Zhao, Z. Yu, C. L. Sun, Z. Wang, N. N. Feng, L. Q. Mai, Y. G. Wang, Y. Y. Xia, *Energy Environ. Sci.* **2020**, 13, 2200.
- [48] L. K. Gao, X. Cui, Z. W. Wang, C. D. Sewell, Z. L. Li, S. Liang, M. Y. Zhang, J. Li, Y. J. Hu, Z. Q. Lin, *Proc. Natl. Acad. Sci. U. S. A.* **2021**, 118, e2023421118.
- [49] S. Zhang, S. Gu, Y. Wang, C. Liang, Y. Yu, L. Han, S. Zheng, N. Zhang, X. Liu, J. Zhou, J. Li, *ACS Catal.* **2019**, 9, 7389.
- [50] J. C. Dong, X. G. Zhang, V. Briega-Martos, X. Jin, J. Yang, S. Chen, Z. L. Yang, D. Y. Wu, J. M. Feliu, C. T. Williams, Z. Q. Tian, J. F. Li, *Nat. Energy* **2019**, 4, 60.
- [51] M. Wang, L. Árnadóttir, Z. J. Xu, Z. Feng, *Nano-Micro Lett.* **2019**, 11, 47.
- [52] A. Sivanantham, P. Ganesan, A. Vinu, S. Shanmugam, *ACS Catal.* **2020**, 10, 463.
- [53] X. Ren, C. Wei, Y. M. Sun, X. Z. Liu, F. Q. Meng, X. X. Meng, S. N. Sun, S. B. Xi, Y. H. Du, Z. F. Bi, G. Y. Shang, A. C. Fisher, L. Gu, Z. C. J. Xu, *Adv. Mater.* **2020**, 32, 2001292.
- [54] Y. C. Pi, Y. Xu, L. G. Li, T. Sun, B. L. Huang, L. Z. Bu, Y. H. Ma, Z. W. Hu, C. W. Pao, X. Q. Huang, *Adv. Funct. Mater.* **2020**, 30, 2004375.
- [55] W. H. Lee, J. Yi, H. N. Nong, P. Strasser, K. H. Chae, B. K. Min, Y. J. Hwang, H. S. Oh, *Nanoscale* **2020**, 12, 14903.
- [56] L. K. Wu, W. Y. Wu, J. Xia, H. Z. Cao, G. Y. Hou, Y. P. Tang, G. Q. Zheng, *J. Mater. Chem. A* **2017**, 5, 10669.
- [57] Y. Yuan, S. Adimi, X. Guo, T. Thomas, Y. Zhu, H. Guo, G. S. Priyanga, P. Yoo, J. Wang, J. Chen, P. Liao, J. P. Attfield, M. Yang, *Angew. Chem., Int. Ed.* **2020**, 59, 18036.
- [58] P. Zhai, Y. Zhang, Y. Wu, J. Gao, B. Zhang, S. Cao, Y. Zhang, Z. Li, L. Sun, J. Hou, *Nat. Commun.* **2020**, 11, 5462.
- [59] H. Q. Chu, P. P. Feng, B. W. Jin, G. Ye, S. S. Cui, M. Zheng, G. X. Zhang, M. Yang, *Chem. Eng. J.* **2022**, 433, 133523.
- [60] X. Gao, X. Li, Y. Yu, Z. Kou, P. Wang, X. Liu, J. Zhang, J. He, S. Mu, J. Wang, *Nano Energy* **2021**, 85, 105961.
- [61] M. F. Lu, S. X. Kong, S. C. Yan, P. Zhou, T. Yu, Z. G. Zou, *J. Mater. Chem. A* **2022**, 10, 12391.
- [62] C. Zhao, N. Li, R. Zhang, Z. Zhu, J. Lin, K. Zhang, C. Zhao, *ACS Appl. Mater. Interfaces* **2019**, 11, 47858.

- [63] a) Y. C. Lin, C. H. Chuang, L. Y. Hsiao, M. H. Yeh, K. C. Ho, *ACS Appl. Mater. Interfaces* **2020**, 12, 42634; b) Y. H. Tang, Q. Liu, L. Dong, H. B. Wu, X. Y. Yu, *Appl. Catal. B* **2020**, 266, 118627; c) H. Liang, Z. Cao, C. Xia, F. Ming, W. Zhang, A. H. Emwas, L. Cavallo, H. N. Alshareef, *CCS Chem.* **2021**, 3, 1553.
- [64] Y. Guo, T. Wang, J. Chen, J. Zheng, X. Li, K. Ostrikov, *Adv. Energy Mater.* **2018**, 8, 1800085.
- [65] D. Chen, M. Qiao, Y.-R. Lu, L. Hao, D. Liu, C.-L. Dong, Y. Li, S. Wang, *Angew. Chem., Int. Ed.* **2018**, 57, 8691.
- [66] a) J. Sun, H. Xue, N. Guo, T. Song, Y.-r. Hao, J. Sun, J. Zhang, Q. Wang, *Angew. Chem., Int. Ed.* **2020**, 59, 3544; b) G. Huang, Z. Xiao, R. Chen, S. Wang, *ACS Sustainable Chem. Eng.* **2018**, 6, 15954.
- [67] Y. Zhou, W. Zhang, J. Hu, D. Li, X. Yin, Q. Gao, *ACS Sustainable Chem. Eng.* **2021**, 9, 7390.
- [68] Y. J. Wu, J. Yang, T. X. Tu, W. Q. Li, P. F. Zhang, Y. Zhou, J. F. Li, J. T. Li, S. G. Sun, *Angew. Chem., Int. Ed.* **2021**, 60, 26829.
- [69] Q. He, Y. Wan, H. Jiang, Z. Pan, C. Wu, M. Wang, X. Wu, B. Ye, P. M. Ajayan, L. Song, *ACS Energy Lett.* **2018**, 3, 1373.
- [70] Y. Duan, Z. Y. Yu, S. J. Hu, X. S. Zheng, C. T. Zhang, H. H. Ding, B. C. Hu, Q. Q. Fu, Z. L. Yu, X. Zheng, J. F. Zhu, M. R. Gao, S. H. Yu, *Angew. Chem., Int. Ed.* **2019**, 58, 15772.
- [71] a) H. Liang, A. N. Gandhi, C. Xia, M. N. Hedhili, D. H. Anjum, U. Schwingenschlogl, H. N. Alshareef, *ACS Energy Lett.* **2017**, 2, 1035; b) J. S. Kim, I. Park, E. S. Jeong, K. Jin, W. M. Seong, G. Yoon, H. Kim, B. Kim, K. T. Nam, K. Kang, *Adv. Mater.* **2017**, 29, 1606893.
- [72] J. W. Zhao, Z. X. Shi, C. F. Li, Q. Ren, G. R. Li, *ACS Mater. Lett.* **2021**, 3, 721.
- [73] a) H. J. Song, H. Yoon, B. Ju, D. W. Kim, *Adv. Energy Mater.* **2021**, 11, 2002428; b) H. Sun, Y. Zhu, W. Jung, *Molecules* **2021**, 26, 5476.
- [74] Y. G. Fang, Y. S. Fang, R. Q. Zong, Z. Y. Yu, Y. K. Tao, J. Shao, *J. Mater. Chem. A* **2022**, 10, 1369.
- [75] T. H. Shen, L. Spillane, J. Vavra, T. H. M. Pham, J. Peng, Y. Shao-Horn, V. Tileli, *J. Am. Chem. Soc.* **2020**, 142, 15876.
- [76] P. P. Lopes, D. Y. Chung, X. Rui, H. Zheng, H. Y. He, P. F. B. D. Martins, D. Strmcnik, V. R. Stamenkovic, P. Zapol, J. F. Mitchell, R. F. Klie, N. M. Markovic, *J. Am. Chem. Soc.* **2021**, 143, 2741.
- [77] X. J. Cao, X. Y. Yan, L. Ke, K. Zhao, N. Yan, *ACS Appl. Mater. Interfaces* **2021**, 13, 22009.
- [78] R. H. Zhang, N. Dubouis, M. Ben Osman, W. Yin, M. T. Sougrati, D. A. D. Corte, D. Giaume, A. Grimaud, *Angew. Chem., Int. Ed.* **2019**, 58, 4571.
- [79] Y. B. Chen, Y. M. Sun, M. Y. Wang, J. X. Wang, H. Y. Li, S. B. Xi, C. Wei, P. X. Xi, G. E. Sterbinsky, J. W. Freeland, A. C. Fisher, J. W. Ager, Z. X. Feng, Z. J. C. Xu, *Sci. Adv.* **2021**, 7, eabk1788.
- [80] S. A. Park, K. S. Kim, Y. T. Kim, *ACS Energy Lett.* **2018**, 3, 1110.
- [81] H. Li, Y. Chen, J. Z. Y. Seow, C. Liu, A. C. Fisher, J. W. Ager, Z. J. Xu, *Small Sci.* **2022**, 2, 2100048.
- [82] Y. B. Chen, H. Y. Li, J. X. Wang, Y. H. Du, S. B. Xi, Y. M. Sun, M. Sherburne, J. W. Ager, A. C. Fisher, Z. C. J. Xu, *Nat. Commun.* **2019**, 10, 572.
- [83] L. Yang, K. Zhang, H. Chen, L. Shi, X. Liang, X. Wang, Y. Liu, Q. Feng, M. Liu, X. Zou, *J. Energy Chem.* **2022**, 66, 619.
- [84] Y. Zhou, Y. Li, L. Zhang, L. Zhang, L. Li, J. Tian, M. Wang, J. Xu, B. Dai, Y. Li, *Chem. Eng. J.* **2020**, 394, 124977.
- [85] S. L. Li, Z. C. Li, R. G. Ma, C. L. Gao, L. L. Liu, L. P. Hu, J. L. Zhu, T. M. Sun, Y. F. Tang, D. M. Liu, J. C. Wang, *Angew. Chem., Int. Ed.* **2021**, 60, 3773.
- [86] Q. C. Xu, H. Jiang, X. Z. Duan, Z. Jiang, Y. J. Hu, S. W. Boettcher, W. Y. Zhang, S. J. Guo, C. Z. Li, *Nano Lett.* **2021**, 21, 492.
- [87] Y. Duan, J. Y. Lee, S. B. Xi, Y. M. Sun, J. J. Ge, S. J. H. Ong, Y. B. Chen, S. Dou, F. X. Meng, C. Z. Diao, A. C. Fisher, X. Wang, G. G. Scherer, A. Grimaud, Z. C. J. Xu, *Angew. Chem., Int. Ed.* **2021**, 60, 7418.
- [88] K. Fan, H. Y. Zou, L. L. Duan, L. C. Sun, *Adv. Energy Mater.* **2020**, 10, 1903571.
- [89] Y. C. Pi, Q. Shao, X. Zhu, X. Q. Huang, *ACS Nano* **2018**, 12, 7371.
- [90] Z. J. Chen, R. J. Zheng, M. Gras, W. Wei, G. Lota, H. Chen, B. J. Ni, *Appl. Catal. B* **2021**, 288, 120037.
- [91] B. Jiang, Z. Wan, Y. Q. Kang, Y. N. Guo, J. Henzie, J. Na, H. X. Li, S. Y. Wang, Y. S. Bando, Y. S. Sakka, Y. Yamauchi, *Nano Energy* **2021**, 81, 105644.
- [92] W. J. Dai, X. W. Bai, Y. A. Zhu, Y. Zhang, T. Lu, Y. Pan, J. L. Wang, *J. Mater. Chem. A* **2021**, 9, 6432.
- [93] T. W. Zhao, X. J. Shen, Y. Wang, R. K. Hocking, Y. B. Li, C. L. Rong, K. Dastafkan, Z. Su, C. Zhao, *Adv. Funct. Mater.* **2021**, 31, 2100614.
- [94] T. Tang, W. J. Jiang, S. Niu, N. Liu, H. Luo, Y. Y. Chen, S. F. Jin, F. Gao, L. J. Wan, J. S. Hu, *J. Am. Chem. Soc.* **2017**, 139, 8320.
- [95] Y. X. Lin, L. Yang, H. L. Jiang, Y. K. Zhang, Y. N. Bo, P. Liu, S. M. Chen, B. Xiang, G. Li, J. Jiang, Y. J. Xiong, L. Song, *J. Phys. Chem. Lett.* **2020**, 11, 1746.
- [96] L. Wang, Q. Zhou, Z. H. Pu, Q. Zhang, X. Q. Mu, H. Y. Jing, S. L. Liu, C. Y. Chen, S. C. Mu, *Nano Energy* **2018**, 53, 270.
- [97] M. Li, H. Liu, L. Feng, *Electrochem. Commun.* **2021**, 122, 106901.
- [98] F. H. Ma, Q. Wu, M. Liu, L. R. Zheng, F. X. Tong, Z. Y. Wang, P. Wang, Y. Y. Liu, H. F. Cheng, Y. Dai, Z. K. Zheng, Y. C. Fan, B. B. Huang, *ACS Appl. Mater. Interfaces* **2021**, 13, 5142.
- [99] P. Z. Chen, T. P. Zhou, S. B. Wang, N. Zhang, Y. Tong, H. X. Ju, W. S. Chu, C. Z. Wu, Y. Xie, *Angew. Chem., Int. Ed.* **2018**, 57, 15471.
- [100] J. Wang, S. J. Kim, J. P. Liu, Y. Gao, S. Choi, J. Han, H. Shin, S. Jo, J. Kim, F. Ciucci, H. Kim, Q. T. Li, W. L. Yang, X. Long, S. H. Yang, S. P. Cho, K. H. Chae, M. G. Kim, H. Kim, J. Lim, *Nat. Catal.* **2021**, 4, 212.
- [101] T. Z. Wu, S. N. Sun, J. J. Song, S. B. Xi, Y. H. Du, B. Chen, W. A. Sasangka, H. B. Liao, C. L. Gan, G. G. Scherer, L. Zeng, H. J. Wang, H. Li, A. Grimaud, Z. J. Xu, *Nat. Catal.* **2019**, 2, 763.
- [102] Y. Sun, R. Li, X. X. Chen, J. Wu, Y. Xie, X. Wang, K. K. Ma, L. Wang, Z. Zhang, Q. L. Liao, Z. Kang, Y. Zhang, *Adv. Energy Mater.* **2021**, 11, 2003755.
- [103] W. F. Peng, J. K. Li, K. Q. Shen, L. R. Zheng, H. Tang, Y. T. Gong, J. S. Zhou, N. Chen, S. J. Zhao, M. Y. Chen, F. M. Gao, H. Y. Gou, *J. Mater. Chem. A* **2020**, 8, 23580.
- [104] X. Zhao, Y. L. Xing, L. Y. Zhao, S. C. Lu, F. Ahmad, J. Zeng, *J. Catal.* **2018**, 368, 155.
- [105] L. Trotochaud, S. L. Young, J. K. Ranney, S. W. Boettcher, *J. Am. Chem. Soc.* **2014**, 136, 6744.
- [106] J. Bai, J. Mei, T. Liao, Q. Sun, Z. G. Chen, Z. Q. Sun, *Adv. Energy Mater.* **2022**, 12, 2103247.
- [107] a) Z. Hui, Y. Zhong-Yong, *J. Energy Chem.* **2020**, 54, 89; b) Y. Liu, J. Wang, S. Kim, H. Sun, F. Yang, Z. Fang, N. Tamura, R. Zhang, X. Song, J. Wen, *Nature* **2019**, 570, 358.
- [108] C. Zhang, P. Zhai, M. Xia, Y. Wu, B. Zhang, Z. Li, L. Ran, J. Gao, X. Wang, Z. Fan, L. Sun, J. Hou, *Angew. Chem., Int. Ed.* **2021**, 60, 27126.
- [109] N. Li, L. Cai, C. Wang, Y. Lin, J. Huang, H. Sheng, H. Pan, W. Zhang, Q. Ji, H. Duan, W. Hu, W. Zhang, F. Hu, H. Tan, Z. Sun, B. Song, S. Jin, W. Yan, *J. Am. Chem. Soc.* **2021**, 143, 18001.
- [110] Z. K. Kou, Y. Yu, X. M. Liu, X. R. Gao, L. R. Zheng, H. Y. Zou, Y. J. Pang, Z. Y. Wang, Z. H. Pan, J. Q. He, S. J. Pennycook, J. Wang, *ACS Catal.* **2020**, 10, 4411.
- [111] J. Z. Huang, H. Y. Sheng, R. D. Ross, J. C. Han, X. J. Wang, B. Song, S. Jin, *Nat. Commun.* **2021**, 12, 3036.
- [112] Y. Yi, Q. Wu, J. Li, W. Yao, C. Cui, *ACS Appl. Mater. Interfaces* **2021**, 13, 17439.
- [113] a) Y. Zeng, J. Z. Liao, B. B. Wei, Z. Huang, W. J. Zhu, J. X. Zheng, H. F. Liang, Y. Z. Zhang, Z. C. Wang, *Chem. Eng. J.* **2021**, 409, 7; b) Y. Zeng, Z. Cao, J. Liao, H. Liang, B. Wei, X. Xu, H. Xu, J. Zheng, W. Zhu, L. Cavallo, Z. Wang, *Appl. Catal. B* **2021**, 292, 120160.

- [114] X. R. Gao, X. M. Liu, W. J. Zang, H. L. Dong, Y. J. Pang, Z. K. Kou, P. Y. Wang, Z. H. Pan, S. R. Wei, S. C. Mu, J. Wang, *Nano Energy* **2020**, *78*, 105355.
- [115] P. Guo, Z. J. Wang, S. H. Ge, H. Y. Chen, J. B. Zhang, H. W. Wang, S. Y. Liu, S. X. Wei, X. Q. Lu, *ACS Sustainable Chem. Eng.* **2020**, *8*, 4773.
- [116] A. R. Akbashev, L. Zhang, J. T. Mefford, J. Park, B. Butz, H. Luftman, W. C. Chueh, A. Vojvodic, *Energy Environ. Sci.* **2018**, *11*, 1762.
- [117] L. Huang, G. Gao, H. Zhang, J. X. Chen, Y. X. Fang, S. J. Dong, *Nano Energy* **2020**, *68*, 104296.
- [118] G. S. Tang, Y. Zeng, B. B. Wei, H. F. Liang, J. Wu, P. C. Yao, Z. C. Wang, *Energy Technol.* **2019**, *7*, 1900066.
- [119] J. Choi, D. Kim, W. R. Zheng, B. Y. Yan, Y. Li, L. Y. S. Lee, Y. Piao, *Appl. Catal. B* **2021**, *286*, 119857.
- [120] K. Rui, G. Q. Zhao, Y. P. Chen, Y. Lin, Q. Zhou, J. Y. Chen, J. X. Zhu, W. P. Sun, W. Huang, S. X. Dou, *Adv. Funct. Mater.* **2018**, *28*, 1801554.
- [121] W. R. Zheng, M. J. Liu, L. Y. S. Lee, *ACS Catal.* **2020**, *10*, 81.
- [122] S. J. Hou, W. J. Li, S. Watzele, R. M. Kluge, S. Xue, S. S. Yin, X. Y. Jiang, M. Dobliger, A. Welle, B. Garlyyev, M. Koch, P. Muller-Buschbaum, C. Woll, A. S. Bandarenka, R. A. Fischer, *Adv. Mater.* **2021**, *33*, 2103218.
- [123] S. Ye, Y. Lei, T. Xu, L. Zheng, Z. Chen, X. Yang, X. Ren, Y. Li, Q. Zhang, J. Liu, *Appl. Catal. B* **2022**, *304*, 120986.
- [124] X. Liu, J. Meng, K. Ni, R. Guo, F. Xia, J. Xie, X. Li, B. Wen, P. Wu, M. Li, J. Wu, X. Wu, L. Mai, D. Zhao, *Cell Rep. Phys. Sci.* **2020**, *1*, 100241.
- [125] J. Kwon, H. Han, S. Jo, S. Choi, K. Y. Chung, G. Ali, K. Park, U. Paik, T. Song, *Adv. Energy Mater.* **2021**, *11*, 2100624.
- [126] Y. Wang, Y. L. Zhu, S. L. Zhao, S. X. She, F. F. Zhang, Y. Chen, T. Williams, T. Gengenbach, L. H. Zu, H. Y. Mao, W. Zhou, Z. P. Shao, H. T. Wang, J. Tang, D. Y. Zhao, C. Selomulya, *Matter* **2020**, *3*, 2124.
- [127] X. Liu, F. Y. Xia, R. T. Guo, M. Huang, J. S. Meng, J. S. Wu, L. Q. Mai, *Adv. Funct. Mater.* **2021**, *31*, 2101792.
- [128] X. Liu, R. T. Guo, K. Ni, F. J. Xia, C. J. Niu, B. Wen, J. S. Meng, P. J. Wu, J. S. Wu, X. J. Wu, L. Q. Mai, *Adv. Mater.* **2020**, *32*, 2001136.
- [129] X. Liu, K. Ni, B. Wen, R. T. Guo, C. J. Niu, J. S. Meng, Q. Li, P. J. Wu, Y. W. Zhu, X. J. Wu, L. Q. Mai, *ACS Energy Lett.* **2019**, *4*, 2585.
- [130] G. Chen, Z. W. Hu, Y. P. Zhu, B. B. Gu, Y. J. Zhong, H. J. Lin, C. T. Chen, W. Zhou, Z. P. Shao, *Adv. Mater.* **2018**, *30*, 1804333.
- [131] Y. Y. Wu, Y. Li, M. K. Yuan, H. R. Hao, X. J. San, Z. Lv, L. L. Xu, B. Wei, *Chem. Eng. J.* **2022**, *427*, 131944.
- [132] W. W. Zou, C. L. Sun, K. N. Zhao, J. T. Li, X. L. Pan, D. X. Ye, Y. P. Xie, W. W. Xu, H. B. Zhao, L. Zhang, J. J. Zhang, *Electrochim. Acta* **2020**, *345*, 136114.
- [133] K. Fan, H. Y. Zou, N. V. R. A. Dharanipragada, L. Z. Fan, A. K. Inge, L. L. Duan, B. B. Zhang, L. C. Sun, *J. Mater. Chem. A* **2021**, *9*, 11359.
- [134] Q. R. Zhang, Z. L. Z. Ru, R. Daiyan, P. Kumar, J. Pan, X. Y. Lu, R. Amal, *ACS Appl. Mater. Interfaces* **2021**, *13*, 53798.
- [135] L. Su, X. Cui, T. He, L. Zeng, H. Tian, Y. Song, K. Qi, B. Y. Xia, *Chem. Sci.* **2019**, *10*, 2019.
- [136] S. Bai, M. Xie, T. Cheng, K. Cao, Y. Xu, X. Huang, *Nano Energy* **2020**, *78*, 105224.
- [137] L. He, W. Zhang, Q. Mo, W. Huang, L. Yang, Q. Gao, *Angew. Chem., Int. Ed.* **2020**, *59*, 3544.
- [138] S. Zhang, W. Wang, F. Hu, Y. Mi, S. Wang, Y. Liu, X. Ai, J. Fang, H. Li, T. Zhai, *Nano-Micro Lett.* **2020**, *12*, 140.
- [139] D. Z. Xiao, Q. D. Ruan, D. L. Bao, Y. Luo, C. Huang, S. Y. Tang, J. Shen, C. Cheng, P. K. Chu, *Small* **2020**, *16*, 2001470.
- [140] Y. D. Qu, H. Medina, S. W. Wang, Y. C. Wang, C. W. Chen, T. Y. Su, A. Manikandan, K. Y. Wang, Y. C. Shih, J. W. Chang, H. C. Kuo, C. Y. Lee, S. Y. Lu, G. Z. Shen, Z. M. M. Wang, Y. L. Chueh, *Adv. Mater.* **2016**, *28*, 9831.
- [141] H. Liu, S. Cao, J. Zhang, S. Liu, C. Chen, Y. Zhang, S. Wei, Z. Wang, X. Lu, *Mater. Today Phys.* **2021**, *20*, 100448.
- [142] J. Yu, X. H. Wu, D. Q. Guan, Z. W. Hu, S. C. Weng, H. N. Sun, Y. F. Song, R. Ran, W. Zhou, M. Ni, Z. P. Shao, *Chem. Mater.* **2020**, *32*, 4509.
- [143] L. J. Zhang, H. Jang, Z. J. Li, H. H. Liu, M. G. Kim, X. Liu, J. P. Cho, *Chem. Eng. J.* **2021**, *419*, 129604.
- [144] Q. Quan, X. M. Bu, D. Chen, F. Wang, X. L. Kang, W. Wang, Y. Meng, S. Yip, C. T. Liu, J. C. Ho, *J. Mater. Chem. A* **2022**, *10*, 3953.
- [145] C. F. Yang, W. D. Zhong, K. Shen, Q. Zhang, R. Zhao, H. Xiang, J. Wu, X. K. Li, N. J. Yang, *Adv. Energy Mater.* **2022**, *12*, 2200077.
- [146] H. M. Jiang, L. T. Yan, S. Zhang, Y. C. Zhao, X. Yang, Y. M. Wang, J. X. Shen, X. B. Zhao, L. Z. Wang, *Nano-Micro Lett.* **2021**, *13*, 215.
- [147] P. X. Ji, R. H. Yu, P. Y. Wang, X. L. Pan, H. H. Jin, D. Y. Zheng, D. Chen, J. W. Zhu, Z. H. Pu, J. S. Wu, S. C. Mu, *Adv. Sci.* **2022**, *9*, 2103567.
- [148] M. Yang, Y. R. Zhu, Z. Y. Lin, X. T. Yan, B. Dong, Y. N. Zhou, Q. Z. Li, Y. L. Zhou, J. Nan, Y. M. Chai, *Nanoscale* **2020**, *12*, 12364.
- [149] Y. Sun, J. Wu, Z. Zhang, Q. L. Liao, S. C. Zhang, X. Wang, Y. Xie, K. K. Ma, Z. Kang, Y. Zhang, *Energy Environ. Sci.* **2022**, *15*, 633.
- [150] P. X. Ji, R. H. C. Chen, C. S. Hsu, T. S. Lin, C. J. Chang, S. C. Chang, L. D. Tsai, H. M. Chen, *ACS Energy Lett.* **2019**, *4*, 987.
- [151] H. B. Liao, C. Wei, J. X. Wang, A. Fisher, T. Sritharan, Z. X. Feng, Z. C. J. Xu, *Adv. Energy Mater.* **2017**, *7*, 1701129.
- [152] Z. Xiao, M. Yang, C. Liu, B. Wang, S. Zhang, J. Liu, Z. Xu, R. Gao, J.-J. Zou, A. Tang, H. Yang, *Nano Energy* **2022**, *98*, 107233.
- [153] Y. G. Zhao, N. Dongfang, C. A. Triana, C. Huang, R. Erni, W. C. Wan, J. G. Li, D. Stoian, L. Pan, P. Zhang, J. G. Lan, M. Iannuzzi, G. R. Patzke, *Energy Environ. Sci.* **2022**, *15*, 727.
- [154] J. He, F. Liu, Y. Chen, X. Liu, X. Zhang, L. Zhao, B. Chang, J. Wang, H. Liu, W. Zhou, *Chem. Eng. J.* **2022**, *432*, 134331.
- [155] L. Yuan, S. Liu, S. C. Xu, X. F. Yang, J. L. Bian, C. C. Lv, Z. Y. Yu, T. He, Z. P. Huang, D. W. Boukhvalov, C. W. Cheng, Y. Q. Huang, C. Zhang, *Nano Energy* **2021**, *82*, 105732.
- [156] C. C. Lv, S. C. Xu, Q. P. Yang, Z. P. Huang, C. Zhang, *J. Mater. Chem. A* **2019**, *7*, 12457.
- [157] C. Xie, W. Chen, S. Q. Du, D. F. Yan, Y. Q. Zhang, J. Chen, B. Liu, S. Y. Wang, *Nano Energy* **2020**, *71*, 104653.
- [158] a) Y. X. Guo, C. S. Shang, E. K. Wang, *J. Mater. Chem. A* **2017**, *5*, 2504; b) C. Huang, B. A. Zhang, Y. Z. Wu, Q. D. Ruan, L. L. Liu, J. J. Su, Y. Q. Tang, R. G. Liu, P. K. Chu, *Appl. Catal. B* **2021**, *297*, 120461.
- [159] A. Zhang, Y. Liang, H. Li, B. Zhang, Z. Liu, Q. Chang, H. Zhang, C.-F. Zhu, Z. Geng, W. Zhu, J. Zeng, *Nano Lett.* **2020**, *20*, 8229.
- [160] L. M. Luo, W. Zhan, R. H. Zhang, D. Chen, Q. Y. Hu, Y. F. Guo, X. W. Zhou, *J. Power Sources* **2019**, *412*, 142.
- [161] Y. Lin, L. Yang, H. Jiang, Y. Zhang, Y. Bo, P. Liu, S. Chen, B. Xiang, G. Li, J. Jiang, Y. Xiong, L. Song, *J. Phys. Chem. Lett.* **2020**, *11*, 1746.



Ye Zeng is a 3rd year Ph.D. candidate under the supervision of Prof. Hanfeng Liang in Xiamen University. His research mainly focuses on ration design of earth-abundant materials for energy storage and catalysis.



Qiu Jiang is an associate professor in the School of Materials and Energy at University of Electronic Science and Technology of China (UESTC). He obtained his PhD at King Abdullah University of Science and Technology in 2019 followed by a postdoc at University of Cambridge. His research interests focus on developing methods for controlled synthesis of 2D materials, understanding their fundamental properties, and surface modifications of those materials for energy storage and conversion applications.



Hanfeng Liang received his Ph.D. (2015) from Xiamen University, China. He joined Xiamen University as an associate professor in 2020 after postdoc at King Abdullah University of Science and Technology (KAUST), Saudi Arabia. He currently serves as a Section Associate Editor of Frontiers in Materials and is on the (youth) editorial board of several journals. His research focuses on nanomaterials and functional coatings as well as their application in electrocatalysis and energy storage. He has published over 70 papers with >8000 citations (h-index 39).